GEOMETRY, KINEMATICS AND ACTIVITY OF THE FAULT ZONE AMONG ANKARA-ÇANKIRI

A THESIS SUBMITTED TO
THE GRADUATE SCHOOL OF NATURAL AND APPLIED SCIENCES
OF
MIDDLE EAST TECHNICAL UNIVERSITY

BY

FATMA MELİS BAYINDIR

IN PARTIAL FULFILLMENT OF THE REQUIREMENTS
FOR
THE DEGREE OF MASTER OF SCIENCE
IN
GEOLOGICAL ENGINEERING

AUGUST 2019

Approval of the thesis:

GEOMETRY, KINEMATICS AND ACTIVITY OF THE FAULT ZONE AMONG ANKARA-ÇANKIRI

submitted by **FATMA MELIS BAYINDIR** in partial fulfillment of the requirements for the degree of **Master of Science in Geological Engineering Department, Middle East Technical University** by,

Prof. Dr. Halil Kalıpçılar
Dean, Graduate School of **Natural and Applied Sciences** ________________

Prof. Dr. Erdin Bozkurt
Head of Department, **Geological Engineering** ________________

Prof. Dr. F. Bora Rojay
Supervisor, **Geological Engineering, METU** ________________

Prof. Dr. M. Lütfi Süzen
Co-Supervisor, **Geological Engineering, METU** ________________

Examining Committee Members:

Prof. Dr. Erdin Bozkurt
Geological Engineering, METU ________________

Prof. Dr. F. Bora Rojay
Geological Engineering, METU ________________

Prof. Dr. M. Lütfi Süzen
Geological Engineering, METU ________________

Prof. Dr. Veysel Işık
Geological Engineering, Ankara University ________________

Assist. Prof. Dr. Fatma Toksoy Köksal
Geological Engineering, METU ________________

Date: 28.08.2019

I hereby declare that all information in this document has been obtained and presented in accordance with academic rules and ethical conduct. I also declare that, as required by these rules and conduct, I have fully cited and referenced all material and results that are not original to this work.

Name, Surname: Fatma Melis Bayındır

Signature:

ABSTRACT

GEOMETRY, KINEMATICS AND ACTIVITY OF THE FAULT ZONE AMONG ANKARA-ÇANKIRI

Bayındır, Fatma Melis
Master of Science, Geological Engineering
Supervisor: Prof. Dr. F. Bora Rojay
Co-Supervisor: Prof. Dr. M. Lütfi Süzen

August 2019, 64 pages

Tectonic movements which took place in Late Cretaceous-Neogene time interval make the geology of Central Anatolia very complicated. This study has been carried out to reveal the structural elements and their relationships in this complex geology by taking the advantages of remote sensing in being economical, saving time, having a wide coverage area, detecting the features unseen by naked eye, and being able to observe the areas hard to be reached.

Within the scope of the thesis, evaluation of aerial photos, contrast enhancement, principal component analysis, decorrelation stretching, and stereoscopic image analysis of Terra ASTER data were used as remote sensing methods. Besides, digital elevation modeling and map preparation were used as GIS techniques. In conclusion, lineament analysis, field verification, structural data collection, evaluation of the distinctive points, kinematic interpretation and drawing conclusions from them are the studies that were performed.

The structural elements obtained in the laboratory were controlled in situ and collected slip data were analyzed to make a kinematic interpretation. According to this, it was concluded that the normal faulting overprints onto compressional structures -strike slip faults and thrusts- in Central Anatolia.

Keywords: Remote Sensing, Terra ASTER, Active Fault, Central Anatolia

ÖZ

ANKARA-ÇANKIRI ARASINDAKİ BÖLGENİN GEOMETRİSİ, KİNEMATİĞİ VE AKTİVİTESİ

Bayındır, Fatma Melis
Yüksek Lisans, Jeoloji Mühendisliği
Tez Danışmanı: Prof. Dr. F. Bora Rojay
Ortak Tez Danışmanı: Prof. Dr. M. Lütfi Süzen

Ağustos 2019, 64 sayfa

Geç Kretase-Neojen zaman aralığında gerçekleşen tektonik hareketler, Orta Anadolu'nun jeolojisini oldukça karmaşık hale getirmektedir. Bu çalışma, bu karmaşık jeolojideki yapısal unsurları ve aralarındaki ilişkiyi uzaktan algılamanın sağladığı ekonomik olma, zamandan tasarruf sağlama, geniş kapsama alanına sahip olma, gözle görülemeyen özellikleri tespit edebilme, ulaşılması güç alanları gözleyebilme gibi avantajları kullanarak ortaya koyabilme amacıyla gerçekleştirilmiştir.

Proje kapsamında hava fotoğraflarının değerlendirilmesi, Terra ASTER verisinden kontrast zenginleştirme, temel bileşen analizi, dekorelasyon germesi ve stereoskopik görüntü analizi gibi uzaktan algılama yöntemleri kullanılmıştır. Bunun yanısıra çalışmada sayısal yükseklik modeli oluşturma, harita hazırlama gibi CBS teknikleri kullanılmıştır. Sonuç olarak çizgisellik analizi yapılması, arazi doğrulama, yapısal veri toplama, kinematik yorum yapma ve farklı olan noktaların değerlendirilerek bunlardan sonuç çıkarılması gibi çalışmalar gerçekleştirilmiştir.

Laboratuvarda elde edilen yapısal unsurlar arazide, yerinde kontrol edilmiş ve toplanan kayma verileri kinematik bir yoruma gitmek için analiz edilmiştir. Buna göre, Orta Anadolu’da genişleme ürünü olan normal faylanmanın sıkışma yapılarından - yanal atımlı faylar ve bindirmelerden- sonra geliştiği sonucuna varılmıştır.

Anahtar Kelimeler: Uzaktan Algılama, Terra ASTER, Aktif Fay, Orta Anadolu

To My Beloved Family

ACKNOWLEDGEMENTS

I would like to express my deepest gratitude to my supervisor Prof. Dr. F. Bora Rojay and co-supervisor Prof. Dr. M. Lütfi Süzen for their guidance, comments, encouragements, patience, and insight throughout the research.

I would also like to thank Prof. Dr. Nuretdin Kaymakçı for his advices.

I thank the authorities of the institution that I am a member of, which is General Directorate of Mineral Research and Exploration (MTA), to give me their supports.

I am very grateful to my Head of Departments in MTA and colleagues in MTA Dr. İsmail Seyhan Remote Sensing Center for their continuous motivations.

Finally, I would like to thank my parents, my sister Pelin, my husband Erol for their support, and my son Ali for being joy of my life.

TABLE OF CONTENTS

ABSTRACT v

ÖZ vii

ACKNOWLEDGEMENTS x

TABLE OF CONTENTS xi

LIST OF FIGURES xiii

LIST OF ABBREVIATIONS xvi

LIST OF SYMBOLS xix

CHAPTERS

1. INTRODUCTION 1

    1.1. Purpose and Scope 1

    1.2. Study Area 2

    1.3. Methods of Study 2

2. GEOLOGY 5

    2.1. Regional Geology 5

        2.1.1. Stratigraphy 5

        2.1.2. Structural Geological Elements 9

    2.2. Previous Studies on Tectonics 10

3. GIS STUDIES 13

    3.1. Digital Geology Map 13

    3.2. Digital Elevation Model 13

    3.3. Shaded Relief Map 16

4. REMOTE SENSING STUDIES 17

4.1. Previous Studies 17

4.2. Methods Used 18

4.3. Lineament Analysis 18

4.3.1. Terra ASTER 19

4.3.1.1. Stereoscopic Image 20

4.3.1.2. Atmospheric Correction 21

4.3.1.3. Principal Component Analysis (PCA) 23

4.3.1.4. Decorrelation Stretch 24

5. STRUCTURAL ANALYSIS 29

5.1. Field Verification 29

5.2. Fault Slip Data 29

5.2.1. Win_Tensor Software 32

5.2.2. Interpretations 34

6. DISCUSSION 47

7. CONCLUSIONS 55

REFERENCES 59

LIST OF FIGURES

FIGURES

Figure 1.1. Site location map and satellite image borders involving the study area based on 1:100.000 scaled map indexes. 3
Figure 1.2. Diagram of the methods of the study...4
Figure 2.1. Simplified map of tectonic elements of Anatolia from Ketin 1966, showing main tectonic units, the front of the İzmir-Ankara-Erzincan suture (IAES) belt..6
Figure 2.2. Stratigraphic columnar section (not to scale) of the study area (adapted from Rojay and Karaca 2008)...7
Figure 2.3. Geological and fault maps of the study area based on 1:100.000 scaled MTA geological map and fault map. 8
Figure 2.4. Small scale normal growth faults developed in Miocene mudrocks (Değirmenkaya Village)..9
Figure 3.1. Simplified geological map and the study area.......................................14
Figure 3.2. a. ASTER Global DEM, and b. shaded relief map covering the study area. 15
Figure 4.1. Flowchart of the remote sensing methods used in the study. 18
Figure 4.2. Wavelength and resolutions for ASTER images...................................20
Figure 4.3. Structural element analysis with stereoscopic image 22
Figure 4.4. Generating Principal Component Analysis image with VNIR bands 1, 2, 3...25
Figure 4.5. Generating Principal Component Analysis image with SWIR bands 1, 2, 3, 4, 5, 6...26
Figure 4.6. Generating decorrelation stretching image with all VNIR and SWIR bands 27

Figure 5.1. An example of the field verification study of the linear structural element map obtained from stereoscopic image (Yalaycık, Çankırı). 30
Figure 5.2. Structural elements from fault plane slip data locations in the field. 31
Figure 5.3. Stress ellipsoid. 32
Figure 5.4. Illustration of orientation of principal axes, stress ratio R, and stress behaviours (Delvaux et al. 1997). 33
Figure 5.5. Miocene mudrocks-Cretaceous ophiolitic Melange contact from the NE slope of Karahöyük Village (GPS Location: 530576 E, 4450522 N). 35
Figure 5.6. Win_Tensor data worksheet for location 1 (GPS Location 530576 E, 4450522 N). 35
Figure 5.7. Win_Tensor data worksheet for location 2 (GPS Location: 529349 E, 4453676 N). 36
Figure 5.8. Measurement from the fault plane, location 3 (GPS Location: 533394 E, 4466275 N). 37
Figure 5.9. Win_Tensor data worksheet for location 3 (GPS Location: 3533394 E, 4466275 N). 37
Figure 5.10. Shear plane in Bakırlı Village, location 4 (GPS Location: 532262E, 4479658N). 38
Figure 5.11. Win_Tensor data worksheet for location 4 (GPS Location: 532262 E, 4479658 N). 39
Figure 5.12. Fault slip lines on tuff, location 5 (GPS Location: 532325 N: 4479675 E). 39
Figure 5.13. Win_Tensor data worksheet for location 5 (GPS Location: 532325 N: 4479675 E). 40
Figure 5.14. Shears on tuff on Kayıçivi-Yolkaya Road, location 6 (GPS Location: 536993 E, 4502412 N). 40
Figure 5.15. Win_Tensor data worksheet for location 6 (GPS Location: 532262 E, 4479658 N). 41
Figure 5.16. A meter thick fill along a fault at Korgun-Kayıçivi, location 7 (GPS Location: 538531 E, 4505475N). 42

Figure 5.17. Win_Tensor data worksheet for location 7 (GPS Location: 538531 E, 4505475 N). 42
Figure 5.18. Overview of the stereograms and photos of the locations are shown on simplified geological map (NAF; North Anatolian Fault). 44
Figure 5.19. Normal fault with, coarse pyroclastics on the left and tuffaceous west dipping falling block on the right. 45
Figure 5.20. Shear planes in Miocene on the right side of the road from Koyunbaba to Şemsettin Village (GPS Location: 527056 E, 4462629 N). 45
Figure 6.1. Kinematic interpretation of fault slip data on structural element map derived from stereoscopic image. 49
Figure 6.2. Shaded relief image and structural element map derived from stereoscopic image. 51
Figure 6.3. VNIR PCA image and structural element map derived from stereoscopic image. 52
Figure 6.4. SWIR PCA image and structural element map derived from stereoscopic image. 53
Figure 6.5. Decorrelation stretching image and structural element map derived from stereoscopic image. 54
Figure 7.1. a. Structural element map derived from stereoscopic image, b. Length weighted rose diagram of the lineaments on map a, c. Non-weighted weighted rose diagram of the lineaments on map a. 56

LIST OF ABBREVIATIONS

ABBREVIATIONS

3B	3 Backwards
3-D	Three-Dimensional
3N	3 Nadir
AOM	Ankara Ophiolitic Melange
ASTER	Advanced Spaceborne Thermal Emission and Reflection Radiometer
DECORR	Decorrelation Stretch
DEM	Digital Elevation Model
E	East
EFZ	Eldivan Fault Zone
ENE	East-North East
EPCW	Eldivan-Elmadağ pinched crustal wedge
ESE	East-South East
GIS	Geographic Information System
GPS	Global Positioning System
IAES	İzmir-Ankara-Erzincan Suture
ID	Identity Document
Jura	Jurassic
KEFZ	Kırıkkale-Erbaa Fault Zone

Km	Kilometers
Lat	Latitude
Lon	Longitude
M	Meter
Ma	Mega Annum/Millions of Years
MN	Mammal Neogene
MTA	Maden Tetkik ve Arama
N	North
NAF	North Anatolian Fault
NAFS	North Anatolian Fault System
NAFZ	North Anatolian Fault Zone
NASA	National Aeronautics and Space Administration
NE	North East
NNE	North-North East
NNW	North-North West
NW	North West
PCA	Principal Component Analysis
Plio	Pliocene
RGB	Red Green Blue
S	South
SE	South East
SSE	South-South East

SSW	South-South West
SW	South West
SWIR	Shortwave Infrared
Tan	Tangent
TGF	Tuz Gölü Fault
TIR	Thermal Infrared
TM	Thematic Mapper
USA	United States of America
USGS	United States Geological Survey
UTM	Universal Transverse Mercator
VNIR	Visible and Near-Infrared
W	West
WGS	World Geodetic System
WNW	West-North West
WSW	West-South West

LIST OF SYMBOLS

SYMBOLS

a	Friction coefficient
Mw	Moment magnitude/Mechanical work
R	Stress ratio
v	Normal stress
σ_1	Maximum compression
σ_2	Intermediate compression
σ_3	Minimum compression
σ_i	Isotropic stress
σ_v	Vertical stress
ϕ	Characteristic friction angle
τ	Shear stress
Φ	Ratio between the principal axes

CHAPTER 1

INTRODUCTION

1.1. Purpose and Scope

Neotectonic phase in Anatolia started during Miocene with the closing of Neo-Tethys Ocean which originated the Alpide orogeny. The closure generated the fusion of Oligo-Miocene terranes and initiated continental sedimentation, magmatism, extension and strike-slip faulting which is leading a complex geology in Anatolia (Tüysüz 2005).

The specific purposes of the study are to find the main trends of lineaments which is extracted by remote sensing methods between NAF and Tuzgölü fault, and to conduct fault slip data. On the other hand, the main purpose is to link the lineaments with fault slip data and to understand possible tectonic evolution of Korgun-Bala belt related to closure of Neotethys and post-collisional effects.

In accordance with the aim of the study, the structural elements and their relationships in the complicated geology of Central Anatolia were studied by taking the advantages of remote sensing in being economical, saving time, having a wide coverage area, detecting the features unseen by naked eye, and being able to observe the areas hard to be reached. Moreover, the ground truth of the lineaments was surveyed.

Within the scope of the research, literature survey, GIS, remote sensing, field and after field studies had been carried out.

Within GIS, digital map simplification, digital elevation modeling and shaded relief mapping were operated. Remote sensing studies were executed for lineament analysis. In detail, stereoscopic image generation, principal component analysis, and decorrelation stretching methods were processed on Terra ASTER satellite images.

In fieldwork, ground truth of lineament analysis was realized, and fault slip data was collected from 7 locations. After field study, collected data were processed and analyzed for kinematic analysis.

1.2. Study Area

Study area is at the boundary of 1:100.000 scaled F31, G30, G31, H30, H31, I30, I31 and J30 maps (Figures 1.1.). It involves an area of 6465 km^2. Geological maps are generated from 1:100.000 scaled geological maps of MTA, which are F31 (Uğuz and Sevin 2011), G30 (Sevin and Uğuz 2011), G31 (Sevin and Uğuz 2011), H30 (Dönmez and Akçay 2010), H31 (Sevin et al. 2016), I30 (Dönmez et al. 2008), I31 (Dönmez et al. 2005) and J30 (Akçay et al. 2008). Turkey fault map is also shown on the geological map (Emre et al. 2013).

It has a shape like rhomboid, extending along NNE to SSW. It starts 20 km south of the center of Kastamonu and it continues through the south; Ilgaz, Korgun, Çankırı, Kalecik, Elmadağ, Bala, Paşadağ Village and ends at Büyükkışla Village of Şereflikoçhisar. 4 pieces of ASTER images data, each corresponding to 3600 km^2 area, were processed (Figure 1.1.). After the remote sensing and GIS studies, a field survey of approximately 1200 km^2 around the faults was conducted.

1.3. Methods of Study

In the scope of the study, literature survey, remote sensing, and Geographic Information System (GIS) studies had been done before field work study was realized. It was continued with field work and after fieldwork studies as seen in diagram of the methods of the study (Figure 1.2.).

First of all, former researches regarding regional geology, tectonics and remote sensing about any part of the area were compiled.

Secondly, GIS was used in simplifying 1:100.000 scaled geological maps and creating shaded relief map with ArcGIS 9 and Global Mapper 17.

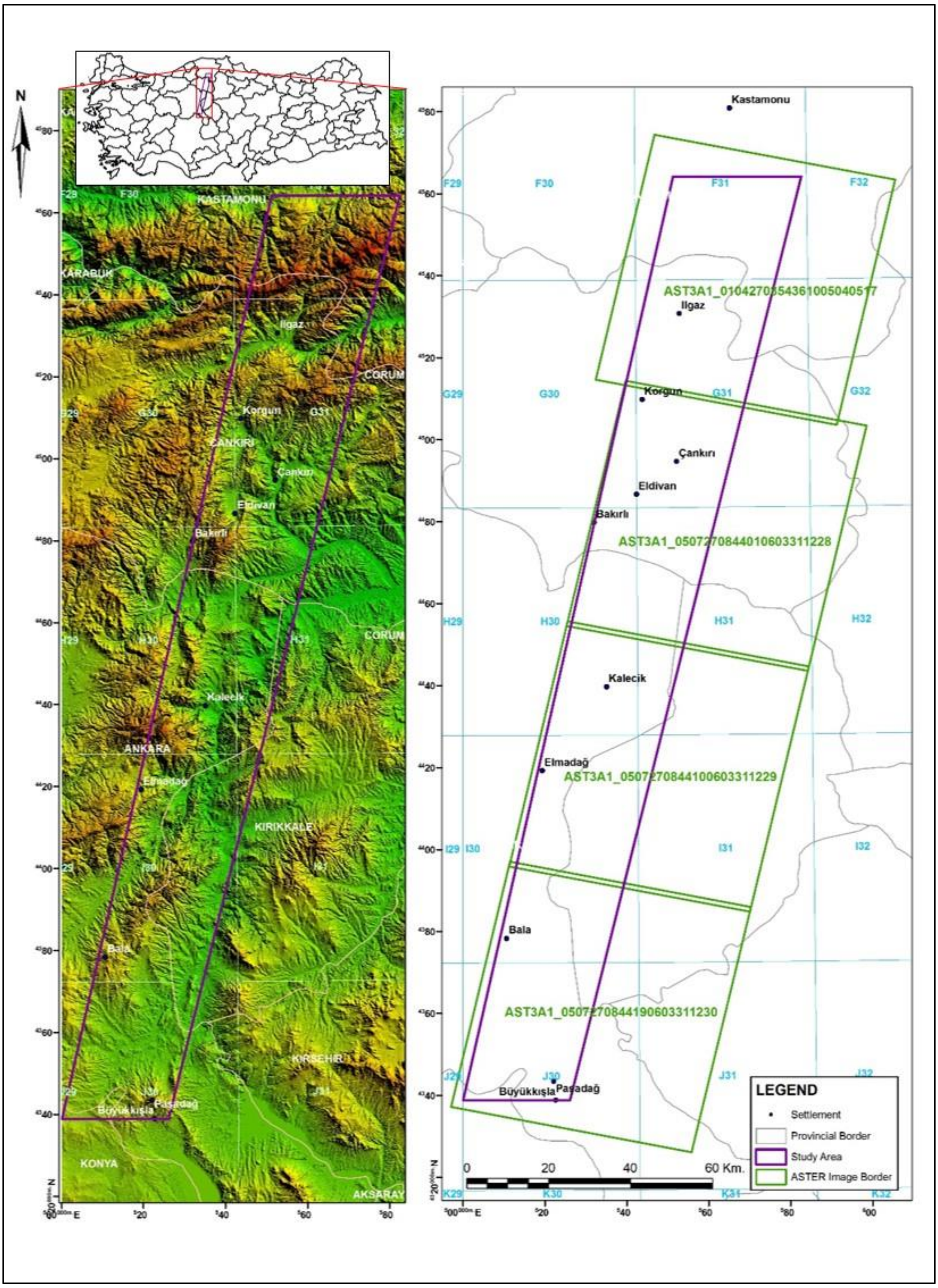

Figure 1.1. Site location map and satellite image borders involving the study area based on 1:100.000 scaled map indexes.

Thirdly, lineament analysis and image enhancement were done using ASTER images with PCI Geomatica 2017 and ERDAS Imagine 9.1 softwares within the scope of remote sensing studies.

Fourthly, in fieldwork study, structural elements which had been derived from lineament analysis were verified and fault slip data was gathered.

Fifthly, after fieldwork, fault slip data were analyzed with Win_Tensor 5.8.5 software and directional data and the frequency of the lineaments were displayed with ArcGIS Polar Plot tool.

Lastly, conducted fault slip data were integrated with the lineament map gathered by using ASTER stereoscopic image.

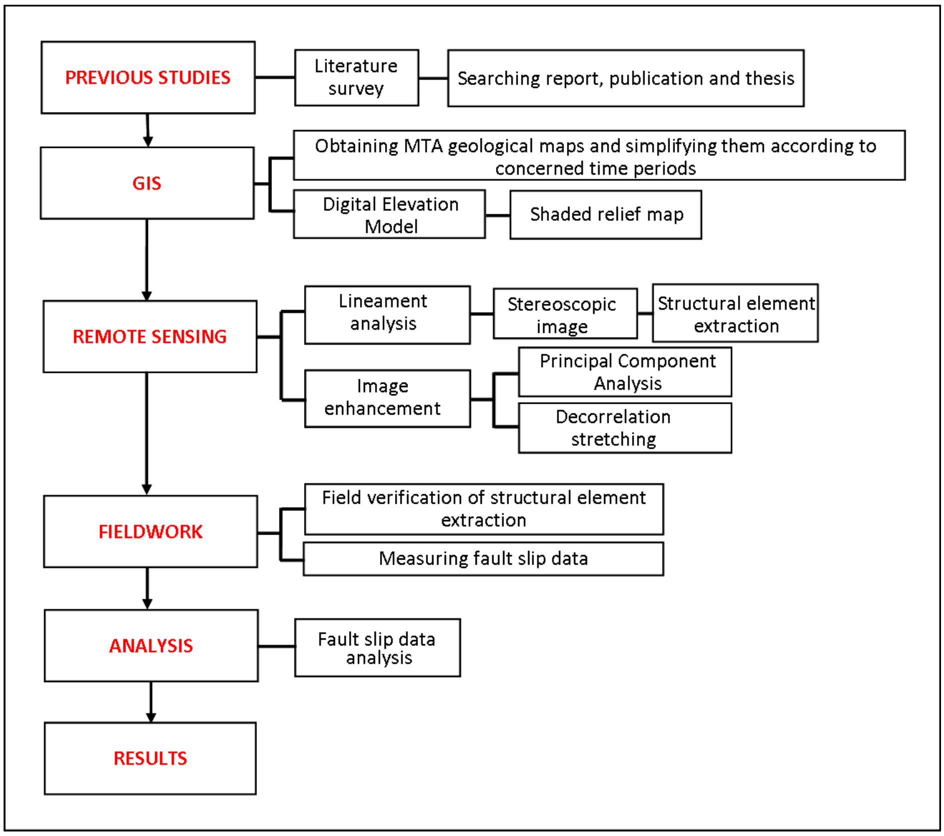

Figure 1.2. Diagram of the methods of the study.

CHAPTER 2

GEOLOGY

2.1. Regional Geology

The study area is located in Central Pontides at the north of the Anatolides-Taurides (Figure 2.1). The selected area is situated along the İzmir-Ankara-Erzincan suture (IAES) belt to the south of North Anatolian Fault (NAF) and north of Ezinepazarı Fault (i.e. Kırıkkale-Erbaa Fault) and northern tip of the Tuzgölü Fault (Okay and Tüysüz 1999).

The belt is an imbricated thrust belt of IAES onto Late Cretaceous to Late Miocene age Çankırı basin (Kaymakci 2000). Belt is constructed of Paleozoic metamorphics, Triassic Karakaya Sequences and Cretaceous ophiolitic mélange thrusted onto Late Cretaceous-Paleogene sequences (Rojay 2013).

The major faults in the region are right-lateral strike-slip NAF in north which is crossing Turkey from east to west, its splay Kırıkkale-Erbaa fault and Tuz Gölü Fault in south (Figure 2.1).

2.1.1. Stratigraphy

The rocks are grouped into two rock packages; i) pre-Miocene basement and ii) Miocene-Quaternary units (Figures 2.2 and 2.3).

The pre-Miocene basement units are composed of Paleozoic metamorphics, Triassic Karakaya sequences, Jurassic-Cretaceous carbonate platform sequences, Upper Cretaceous ophiolitic mélange and Cretaceous sequenes of Cenomanian carbonates to Late Cretaceous flysch, Paleocene clastics, granitoids, Lower Eocene continental-lacustrine sediments, Middle Eocene shallow marine sequence and Oligocene red clastics (Akyürek et al. 1984). These units are overlain by unconformity with the

Lower Miocene fluvials and lacustrine sequences to Plio-Quaternary units. Volcanism cooperates with the sequences in time (Akyürek et al. 1984).

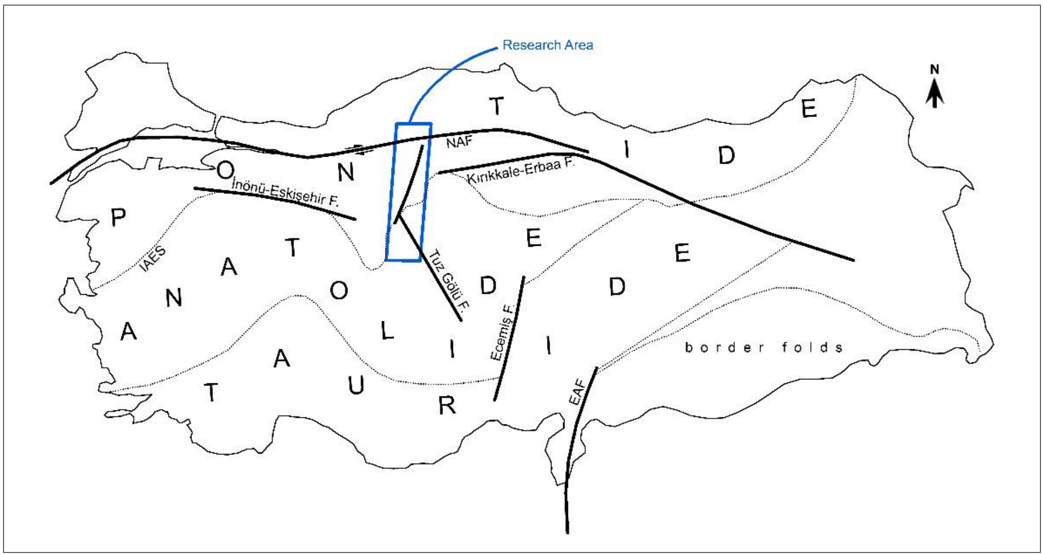

Figure 2.1. Simplified map of tectonic elements of Anatolia from Ketin 1966, showing main tectonic units, the front of the İzmir-Ankara-Erzincan suture (IAES) belt.

Oligo-Miocene thick gypsum sedimentary unit forms an important part of the Miocene stratigraphy in Çankırı region. The upper Lower Miocene-Lower Pliocene (MN4-MN14) succession is overlain by an angular unconformity of Oligo-Miocene age (Kaymakci 2000).

Miocene sequence with extensive volcanism in the region starts with a red cross bedded fluvial sandstone-conglomerate sequence and continues with the lacustrine deposits (MN-4-6(?)). At the highest levels, it ends with creamy white lacustrine mudstone-clayey limestones, sandstones and gypsum, and locally coal beds (MN9-15(?)) (Karaca 2004; Kaymakci 2000). This sequence was intensely deformed and overlain by the red Pliocene-Early Quaternary continental deposits (MN17) with an angular unconformity. The Uppermost Late Miocene (Messinian) is missing in the region. Late Quaternary (Holocene) alluvium and alluvium terraces overlaps Plio-Early Quaternary with an unconformity (Figure 2.2.).

The paleontological studies revealed the existence of MN9- MN13 (11.1 Ma - 6.8 Ma; Agusti et al. 2001) periods (Ozansoy 1961; Akyol 1968; Tatlı 1975; Turgut 1978; Tekkaya 1973; 1974a, b; Şen and Rage 1979; Gürbüz 1981). Beyond the paleontological dating, the existence of the Upper Miocene was supported by the 7.7 ± 0.4 Ma age (Tortonian) dated tuff levels (K-Ar dating of the amphiboles) underlying the gypsiferous levels (Çiner et al. 2011). Moreover, 21 Ma - 25 Ma (Early Miocene) age was obtained with the analysis of the intercalating coal and tuff beds (Türkecan et al. 1991).

The Quaternary overlies the Plio-Early Quaternary deposits with a clear angular unconformity (Karaca 2004).

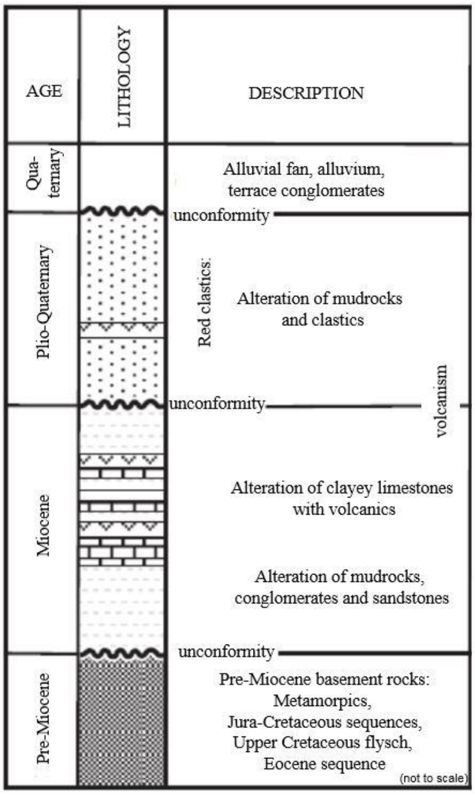

Figure 2.2. Stratigraphic columnar section (not to scale) of the study area (adapted from Rojay and Karaca 2008).

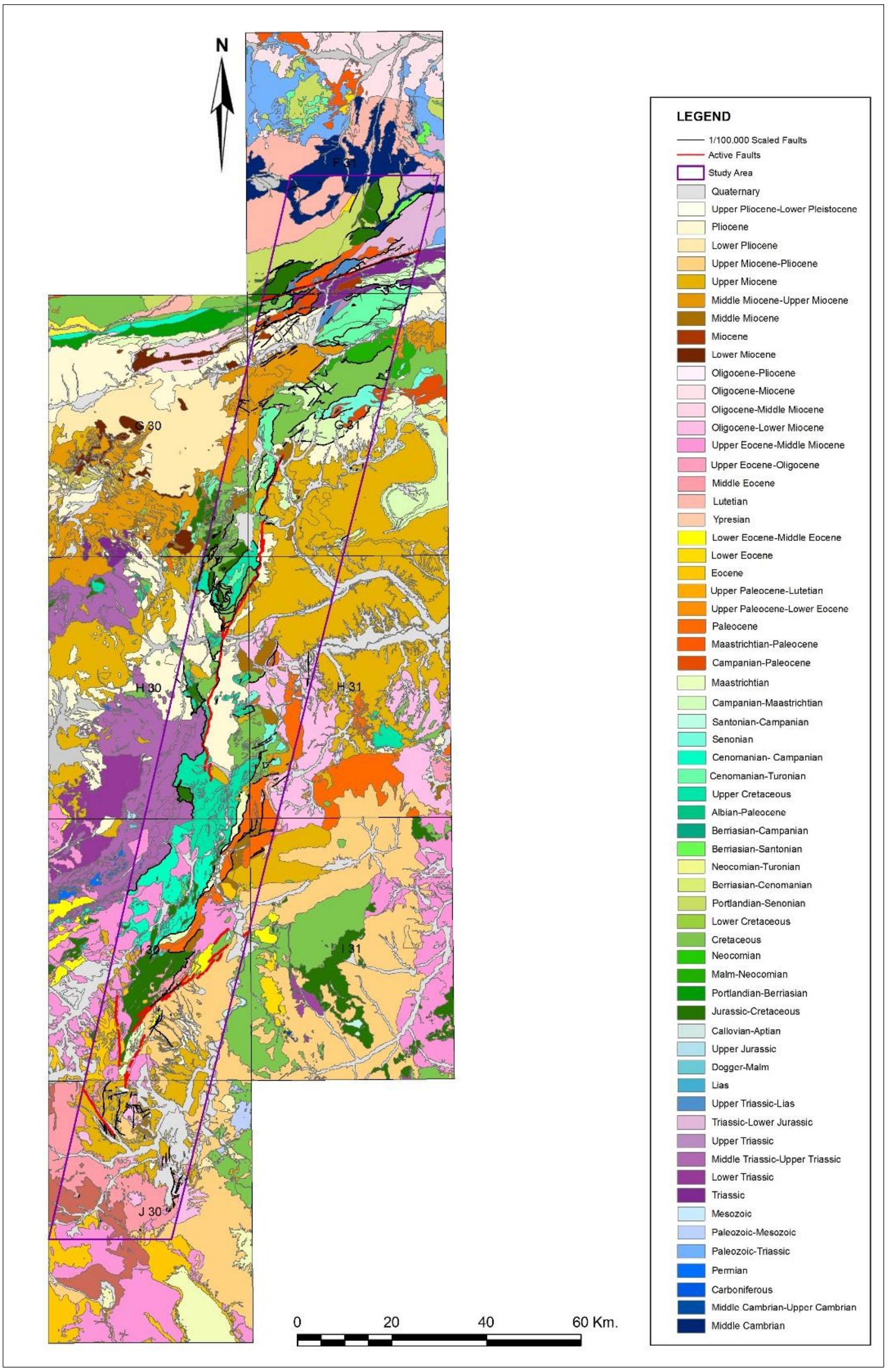

Figure 2.3. Geological and fault maps of the study area based on 1:100.000 scaled MTA geological map and fault map.

2.1.2. Structural Geological Elements

Post-Paleogene was unconformably divided into two Neogene packages as Miocene and Plio-Quaternary deposits in Ankara-Çankırı region. There are also very clear deformational differences between these packages.

The regional deformational periods are; i) post-Miocene–pre-Pliocene, and ii) post-Pliocene periods. The post-Miocene–pre-Pliocene is characterized by intensely folding and thrust-strike slip faulting. On the other hand, Pliocene-Quaternary period is characterized by open-folding, and short-term strike slip faulting followed by normal faulting (Rojay and Karaca 2008).

From the overprinted fault plane data, it is known that the normal faulting overprints onto the strike slip faulting (Rojay and Karaca 2008). In the Plio-Quaternary period, no reverse faulting is observed (Seyitoğlu et al. 1997; Rojay and Karaca 2008). The growth faults that control the sedimentary environment during the Miocene (Figure 2.4.) and Plio-Early Quaternary period are normal faults.

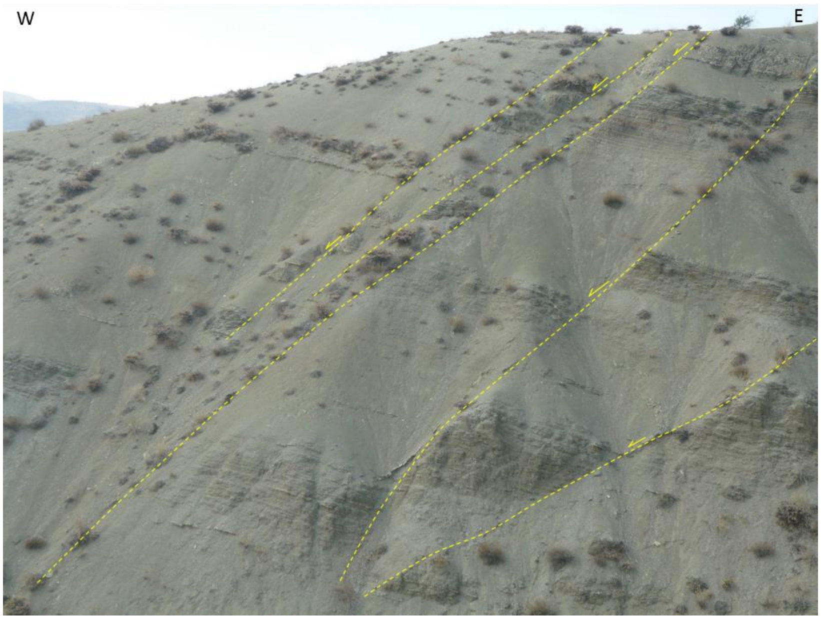

Figure 2.4. Small scale normal growth faults developed in Miocene mudrocks (Değirmenkaya Village).

Normal faulting cross-cuts the alluvium and river terraces and controls their sedimentation.

To sum up, Ankara region developed under approximately N-S compressional and E-W extensional regime after the Miocene, short-term strike slip faulted regime in the Pliocene-Early Quaternary period and then multidirectional extensional regime ranging from NW-SE to WNW-ESE in the post-Early Quaternary period.

In terms of seismic activity, the earthquakes had an impact on Ankara and its surrounding in last century. Some of them are; 19th April 1938 Akpınar (Kırşehir) Earthquake (Mw=6.6), 1st February 1944 Gerede Earthquake (Mw=4.9), 21th April 1983 Köşker (Kulu) Earthquake (Mw=4.7), 6th June 2000 Orta (Çankırı) Earthquake (Mw=6.1), 22nd August 2000 Uruş (Ankara) Earthquake (Mw=4.3), 27th February 2003 Çamlıdere (Ankara) Earthquake (Mw=4.0), 31st July 2005 (Mw=5.2), 20th December 2007 (Mw=5.6), and 27th December 2007 (Mw=5.5) Afşar (Bala-Ankara) Earthquakes. The earthquakes manifests strike slip faulting with normal components to normal faulting (Koçyiğit 2008).

Some of the significant active faults that might be triggering the earthquakes around Ankara are; İnönü-Eskişehir fault, Ayaş, Tuzgölü, Kesikköprü, Küredağ, Balaban and Afşar and Tuzgölü fault.

2.2. Previous Studies on Tectonics

There are various studies dealing with the tectonics of the Central Anatolia.

Some are;

Seyitoğlu et al. (1997) claimed that, an extensional tectonic regime in the Early-Middle Miocene in Central Anatolia at the beginning of the Miocene after post-collisional intracontinental convergence related to the closure of the NeoTethys, before transpressional or transtensional effects of NAFZ.

Kaymakci (2000) proposed an extensional regime model in Çankırı basin during the Early-Middle Miocene with orogenic collapse model, by the fault slip data.

Koçyiğit et al. (2001) used field observations and seismic data to present the activity of the Dodurga fault zone, to express its characteristics and relationships with North Anatolian Fault System, and to clarify the source of the June 6, 2000 Orta earthquake.

Kaymakci et al. (2003), used fault-slip data, overprinting and cross-cutting relationships to clear paleostress history and deformation phases in Çankırı Basin. According to the interpretations, i) escape tectonics continued in late Paleocene to pre-Burdigalian until Early Miocene, ii) Çankırı Basin got extensional tectonic deformation in Middle Miocene, iii) Transcurrent tectonic regime interpreted in the Late Miocene, iv) left lateral Sungurlu Fault Zone was reactivated as right lateral fault and v) Eldivan Fault Zone was reactivated as in left lateral sense during neotectonic period.

Koçyiğit (2008) aimed to mention the earthquake risk in Ankara, source of the 2005-2007 Afşar (Bala-Ankara) earthquakes. In general, NE-trending faults are left lateral strike-slip faults, NW-trending faults are right lateral strike-slip faults, N-S trending faults are oblique slip normal fault with a significant right or left lateral slip component, ENE-trending faults are reverse fault with strike slip component. In summary Bala region is under an impact of conjugate strike slip active faulting evolved under N-S stress regime.

Seyitoğlu et al. (2009) proposed Eldivan-Elmadağ pinched crustal wedge (EPCW) about internal deformation of NW Central Anatolia using geological, seismological and GPS data. EPCW is trending NNE between Çankırı and Ankara bordered with thrust faults in east, and by normal faults in west. It is formed under NW-SE directed compression of NAFZ and Kırıkkale-Erbaa Fault Zone (Seyitoğlu et al. 2000, 2004).

Finally, Esat et al. (2014) investigated Bala earthquakes through the main and aftershock distributions, focal mechanism solutions, detailed geological observations and seismic studies. They comment that the Afşar Fault having a N59°W trending plane is the reason of the main shocks of both the 2005 and 2007 Bala earthquakes and 2005 main shock caused the seismic activity on Karakeçili Fault. Extensional system related to obligue-normal fault segments of Karakeçili Fault terminates at the Afşar Fault which is the northwestern tip of the Tuzgölü Fault Zone.

CHAPTER 3

GIS STUDIES

3.1. Digital Geology Map

A digital geological map is a digitized scanned hardcopy geological map by convenient software adhering to its georeference system.

Topographic maps of 1:100.000 scaled F31, G30, G31, H30, H31, I30, I31, and J30 digital geology maps were supplied from General Directorate of Mineral Research and Exploration. These digital maps are simplified into three groups, namely Plio-Quaternary, Miocene and Pre-Miocene (Figure 3.1.). On the digital maps, the selected groups of rocks are plotted.

3.2. Digital Elevation Model

Digital Elevation Model (DEM) is digital representation of elevation information in a raster or grid form. In this study, DEM is prepared to be a base map to obtain a 3-D topographic map view which is shaded relief map of the study area.

ASTER Global DEM data were used to acquire the digitial elevation model of the area. ASTER Global DEM uses consecutive stereoscopic images of ASTER satellite, having 30 m spatial resolution and high accuracy (NASA, Jet Propulsion Laboratory, 2019). It was downloaded from USGS's website (https://earthexplorer.usgs.gov/). Projection of the data were changed from Geographic (Lat/Lon) to UTM to make compatible with geology maps that we used. DEM which belongs to the area was ready after downloaded data were merged and the output was clipped according to the study area. DEM was created to produce shaded relief map which is a 3-D topographic representation and used to help detecting structural elements (Figure 3.2.).

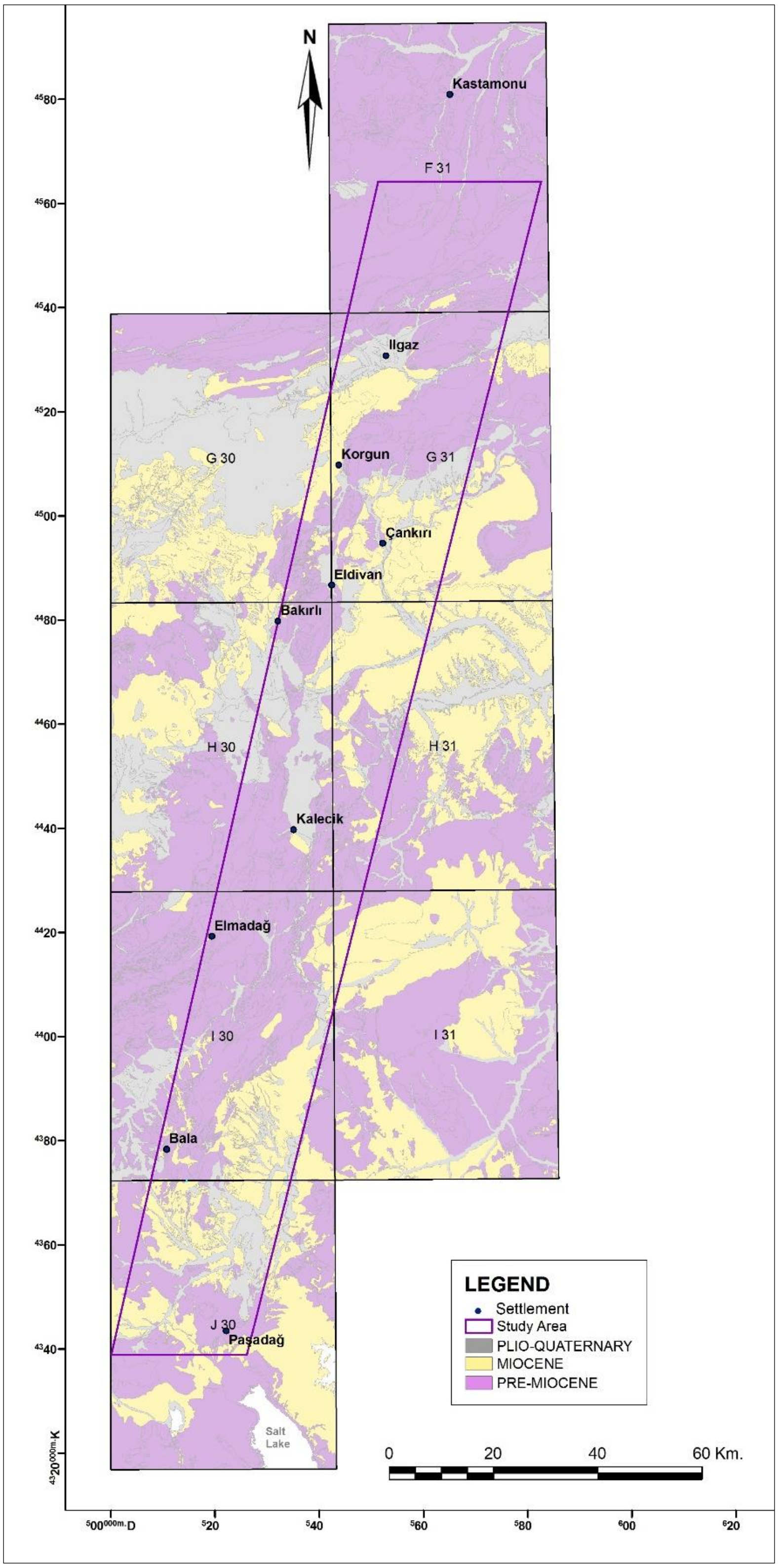

Figure 3.1. Simplified geological map and the study area.

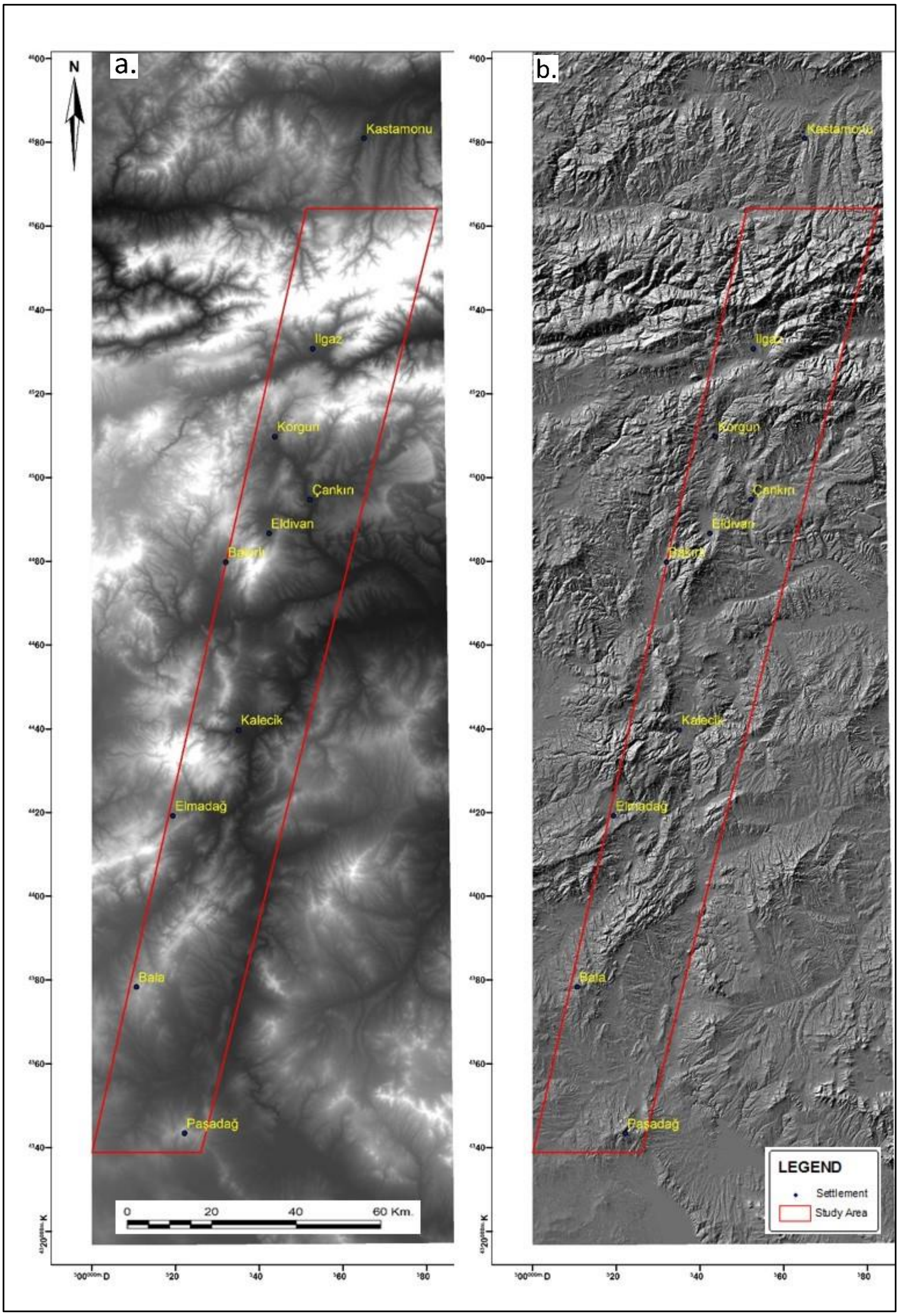

Figure 3.2. a. ASTER Global DEM, and b. shaded relief map covering the study area.

3.3. Shaded Relief Map

A shaded relief map is a 3-dimensional topographic map derived from elevation data of DEM. In this study it was produced to be a control layer for structural element map. Spatial Analyst tool in ArcMap software was used to create shaded relief map.

Hillshade is a kind of surface analysis working with a determined altitude and azimuth values of a hypotetical illumination source processed with slope and aspect calculations, giving illumination values for each raster pixel concerning adjacent cells. Azimuth is the direction of illumination source in angle and altitude is the angle of position of the sun relative to the Earth's horizon in angle (ESRI 2006). In the studty, azimuth and altitude values are specified as 315 and 45 degrees, respectively.

Illumination angle is computed by converting the altitude angle to zenith (straight up) angle, then to radiance. Moreover, illumination angle is calculated by changing the azimuth angle from compass direction to right angle, then to radiance. On the other hand, slope and aspect is evaluated with a center cell of 3x3 cells using x-direction, y-direction, slope and aspect algorithms in relation with its eight neighbors (Burrough and McDonell 1998).

Since a 3-D image was obtained covering the whole area, and it was a useful tool in terms of compatibility of main trends of linear features of the area (Figure 3.2.).

CHAPTER 4

REMOTE SENSING STUDIES

4.1. Previous Studies

There are some previous remote sensing studies within different parts of the study area.

Kaymakci (2000) used remote sensing techniques in his thesis in the interpretation of Çankırı Basin via Landsat TM-5 and analog aerial photos. Formation boundaries, faults, folds and photo-lineaments were interpreted with this study. And trends of lineaments displayed on rose diagrams. Verification was done by fieldwork.

Öztan (2008) in his thesis and, Öztan and Süzen (2011), made a remote sensing study, mapping evaporates in Bala (Ankara) with ASTER data. They modified band combinations in traditional remote sensing methods, namely Band Ratio, Decorrelation Stretch, Crosta technique and Quartz index to discriminate evaporates, especially gypsum which is one of the industrial materials. Fieldwork was done for ground truth. Samples were collected for spectral measurements. Field spectrometer measurements showed compatible results with spectral libraries of the spectrometer software.

Gurcay (2010) used band ratio algorithms of ASTER data to map olivine rich peridotide group among ophiolites around Çankırı region, especially in Eldivan Mountain. Band ratios of TIR give efficient results on discrimination and mapping of olivine-rich unit.

4.2. Methods Used

Remote sensing studies were done using ASTER images with PCI Geomatica 2017 and ERDAS Imagine 9.1 softwares. Lineament analysis was made by generating 3-D view via stereoscopic image and gathering structural element map from stereoscopic image. Image enhancement techniques were also used to emphasize the lithological differences which may be arised from structural differences. Methods that were used in remote sensing studies are shown as a flowchart (Figure 4.1.).

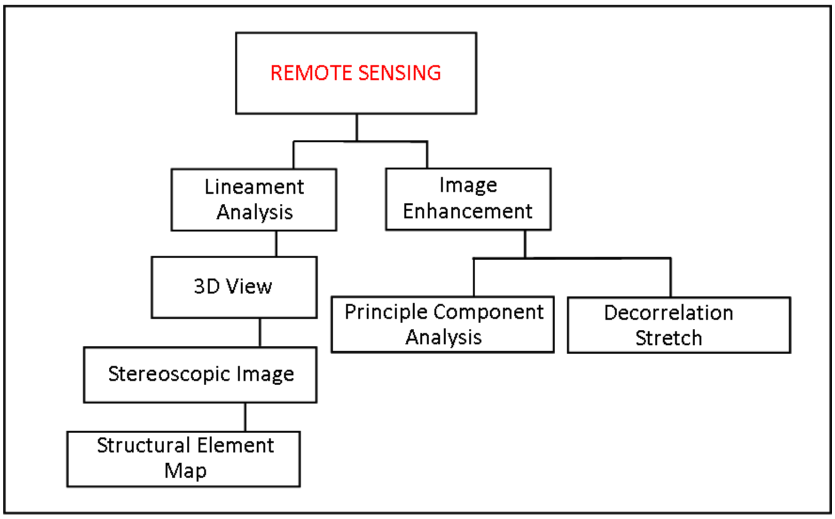

Figure 4.1. Flowchart of the remote sensing methods used in the study.

4.3. Lineament Analysis

Lineament is defined as mappable straight or braided linear features which has different pattern, apart from their environment and presumably reflects a subsurface phenomenon by O'Leary et al. (1976). Moreover, lineament analysis is used for determination of faults and helps the identification of major trends of the area.

In this study, lineaments were supervised manually and digitally based on stereoscopic image which was derived from Terra ASTER data. Additionally, shaded relief map produced by GIS studies, principal component analysis, and decorrelation stretch images from Terra ASTER data were used as supportive control layers for generating lineament map.

Lineaments were drawn digitally on ERDAS IMAGINE 9.1 as a shape layer. Output lineament map analysed with ArcGIS Polar Plot and length weighted and non-weighted, bidirectional rose diagrams were generated in order to determine main direction of lineaments extracted between the North Anatolian Fault in north and continuation of the Tuzgölü Fault in the south.

4.3.1. Terra ASTER

As introduced in ASTER User Handbook (2002), the Advanced Spaceborne Thermal Emission and Reflection Radiometer (ASTER) is an imaging instrument onboard Terra, the flagship satellite of NASA's Earth Observing System. It has three subsystems, having different spatial resolutions varying with wavelength. The sensor has 14 spectral bands— the three is VNIR (in 0.52–0.86 μm spectral range) with 15 m spatial resolution, the six is SWIR (in 1.60–2.43 μm spectral range) with 30 m resolution, and the five is TIR (in 8.125–11.65 μm spectral range) with 90 m resolution (Figure 4.2.). Visible and Near Infrared (VNIR) has three bands and an additional backward telescope for stereoscopic. SWIR is the abbreviation of Shortwave Infrared, and TIR is the abbreviation of Thermal Infrared. Each ASTER scene covers an area of 60 x 60 km^2.

There are 4 Terra ASTER images in the scope of the study. Granule ID’s of the images are AST3A1 0104270854361005040517, AST3A1 0507270844010603311228, AST3A1 0507270844100603311229, and AST3A1 0507270844190603311230.

Both VNIR and SWIR bands were used in the study. For instance, VNIR 3N and 3B were used for creating stereoscopic imagery to 3-D visualization. Two subsystems: namely atmospherically corrected VNIR 1,2,3 and atmospherically corrected SWIR 1,2,3,4,5,6 were operated separately from each other in PCA, and all VNIR and SWIR bands were used in decorrelation stretch method. PCA and decorrelation stretch methods were both utilized to emphasize the lithological differences to find out the possible structural elements that can be originated from these differences.

Spectral Range	Wavelength (µm)	Resolution (m)
Band 1 – Visible Near Infrared	0.52-0.60	15
Band 2 – Visible Near Infrared	0.63-0.69	15
Band 3N – Visible Near Infrared	0.78 - 0.86	15
Band 3B – Visible Near Infrared	0.78 - 0.86	15
Band 4 – Shortwave Infrared	1.60-1.70	30
Band 5 – Shortwave Infrared	2.145-2.185	30
Band 6 – Shortwave Infrared	2.185-2.225	30
Band 7 – Shortwave Infrared	2.235-2.285	30
Band 8 – Shortwave Infrared	2.295-2.365	30
Band 9 – Shortwave Infrared	2.360-2.430	30
Band 10 – Thermal Infrared	8.125-8.475	90
Band 11 – Thermal Infrared	8.475-8.825	90
Band 12 – Thermal Infrared	8.925-9.275	90
Band 13 – Thermal Infrared	10.25-10.95	90
Band 14 – Thermal Infrared	10.95-11.65	90

Figure 4.2. Wavelength and resolutions for ASTER images.

4.3.1.1. Stereoscopic Image

Stereoscopic image is gathered by overlapping images of an area that are captured from two different points of view. Furthermore, a stereoscopic effect is achieved by looking the stereoscopic image with stereoscopic glasses. Left and right eye see the left and right images respectively. This is analogous to the depth perception you achieve by looking at a feature with your two eyes (Leica Geosystems Geospatial Imaging, LLC 2006).

As implied before, VNIR has three bands and an additional backward telescope for stereoscopic capability. Thus, the 3rd band of Terra ASTER sensor takes images of an area from two different points of view, namely nadir (vertically downward, and via band 3N) and backward (via band 3B). These two images processed with stereo module developed in PCI Geomatica Software. Looking the resultant image in R G B: 3B 3N 3N with stereoscopic glasses or red/blue anaglyph glasses, 3D display of the field is acquired. This provides a perceiving of the structural elements as being in the field. Thus, fault markers such as fault scarps, discontinuity of the structures, shapes of water deposits, pressure ridges, elongated hills, deep linear valleys, linear vegetation and etc. on the images guides to draw structural elements before field work.

4 Terra ASTER images corresponding the area were processed separately with stereo module in PCI Geomatica. The obtained images were mosaicked and cropped according to the study area. Output image was displayed on ERDAS IMAGINE 9.1 software as R G B: 3B 3N 3N. It was rotated to 90° clockwise to be seen red/blue glasses and then looked by stereoscopic (red/blue) glasses. Afterwards, structural elements were analyzed on ERDAS IMAGINE 9.1 software in minimum 1:100.000, optimum 1:50.000 and maximum 1:30.000 scales (Figure 4.3.).

4.3.1.2. Atmospheric Correction

Before applying principle component analysis, atmospheric correction was carried out to remove atmospheric effects.

There were some processes need to be done before atmospheric correction. Primarily, geometric correction, in other words ortho-rectification, or georeferencing of satellite image was performed. It was done to transfer the coordinate system of map or another image to satellite image. The coordinate system of the reference map or image should involve at least the area of the image whose coordinate will be changed. Here, 14 pieces of 1:100.000 scaled topographic maps having UTM, WGS 84 coordinate system were used in total for geometric correction of ASTER images. Topographic maps were merged for each image as they enclose it. Afterwards, masking process was applied to georeferenced image. The irrelevant data to our study such as water area, vegetation and cloud were masked.

Spectral Range	Wavelength (µm)	Resolution (m)	Sensing Direction
Band 3N – Visible Near Infrared	0.78-0.86	15	Vertical
Band 3B – Visible Near Infrared	0.78-0.86	15	Backward

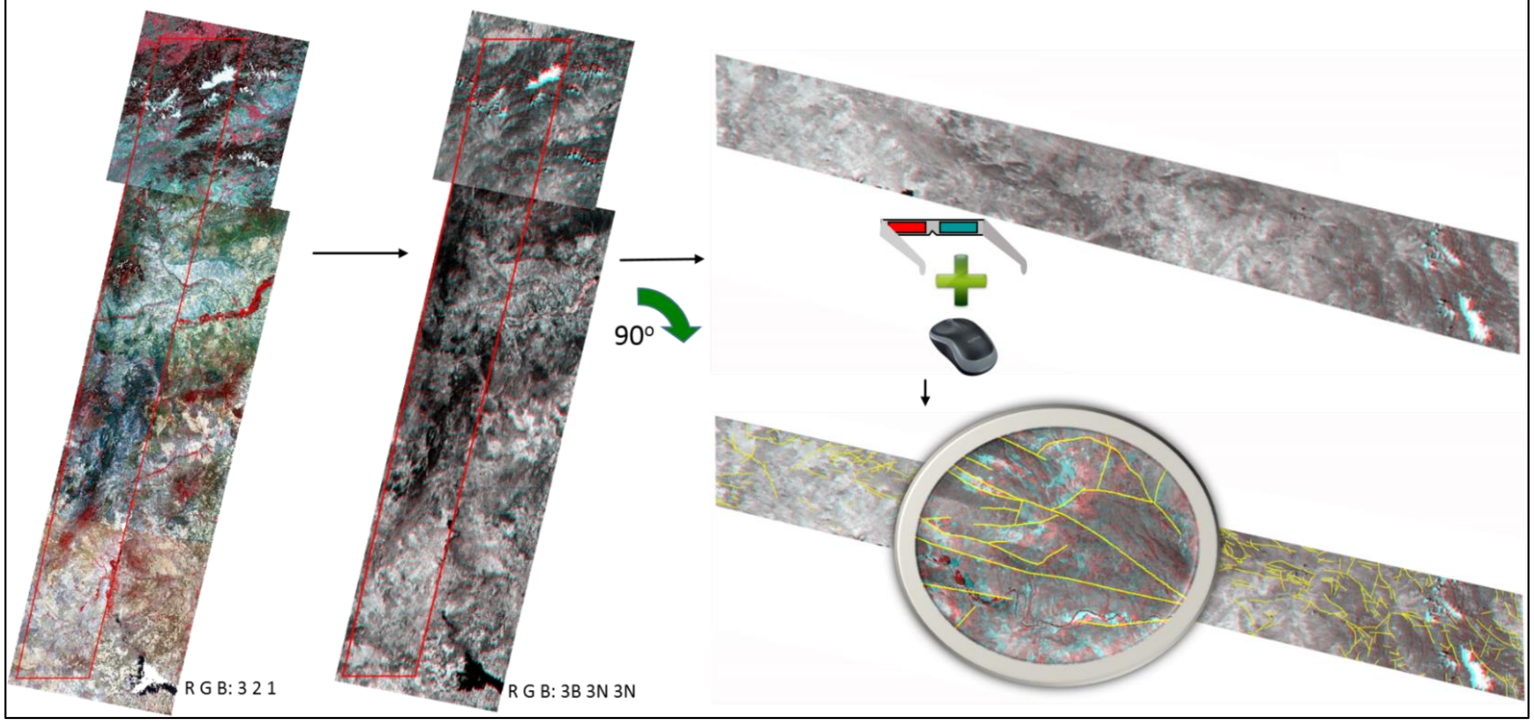

Figure 4.3. Structural element analysis with stereoscopic image.

Next, atmospheric correction was made to reduce the atmospheric effects such as haze and vapor, which exist during receiving the image. Here, Dark Object Subtraction Method was used for atmospheric correction. As Chavez (1996) remarked, it is completely image-based atmospheric correction technique and independent from field measurements. As Crane (1971) imply, dark objects, which are not reflecting light but having digital number greater than zero, occur on the image because of the atmospheric scattering effects. For this reason, every minimum value of each band is greater than zero and atmospheric scattering effects were eliminated by subtraction of the minimum values of all bands from each pixel values.

Radiances measured in wavelengths were converted to digital numbers for ease of storage and transferring the data by sensor. Then digital numbers were again converted into spectral radiance by sensor to get a meaningful spectral signature and unit for surface features. Radiance depends on the illumination (both its intensity and direction), the orientation and position of the target and the path of the light through the atmosphere (Harris Geospatial Solutions 2017). On the other hand, reflectance is the ratio of incident flux to reflected flux, therefore unitless and independent on illumination and aforesaid factors. In other words, conversion to reflectance is due to remove the degree of illumination of the object (i.e. irradiance). Thus, subsequently radiance was converted into at-sensor reflectance to obtain specific reflection values of materials compatible for all images. Then as Ghulam (2009) expresses, surface reflectance was calculated by correlating the field measured surface reflectance with synchronous pixel value. Spectrometers are used to measure field reflectance.

4.3.1.3. Principal Component Analysis (PCA)

Principal Component Analysis (PCA) is an image enhancement technique. As Sabins (1997) implies, it is used for compacting the data content of multi-band data set. Squeezing similar data in a few bands lessens the extent of the data (Jackson 1983) and thus provides new bands which are more appropriate for eye perception.

For principle component analysis, VNIR and SWIR bands of ASTER image were used separately. Principle component analysis was applied to all 3 VNIR bands and then all 6 SWIR bands of 4 different Terra ASTER images, separately. Subsequently water and cloud masking were performed. These 4 images were cut according to the study area, mosaicked, in other words they were merged, and viewed in RGB: 123 and RGB: 456 (Figure 4.4. and 4.5.).

4.3.1.4. Decorrelation Stretch

As in PCI Geomatica Online Manual (2018) declares, decorrelation stretch is a kind of transformation of channels, especially effective on images in which channels are highly correlated (that is, the spectral bands are very similar). Decorrelation is based upon Principal Component Analysis and uses eigenchannels. Decorrelation stretching is a way of modifying, or stretching, the results of a PCA transformation. It greatly increases color saturation and gets more vivid color, greatly exaggerates lithological differences and makes it easier to distinguish the differences of materials on the surface. All VNIR and SWIR bands were selected to be used in DECORR module of PCI Geomatica 2017 software and viewed in in RGB: 246. Eventually, another control layer for manually created structural element map with stereoscopic image was produced (Figure 4.6.).

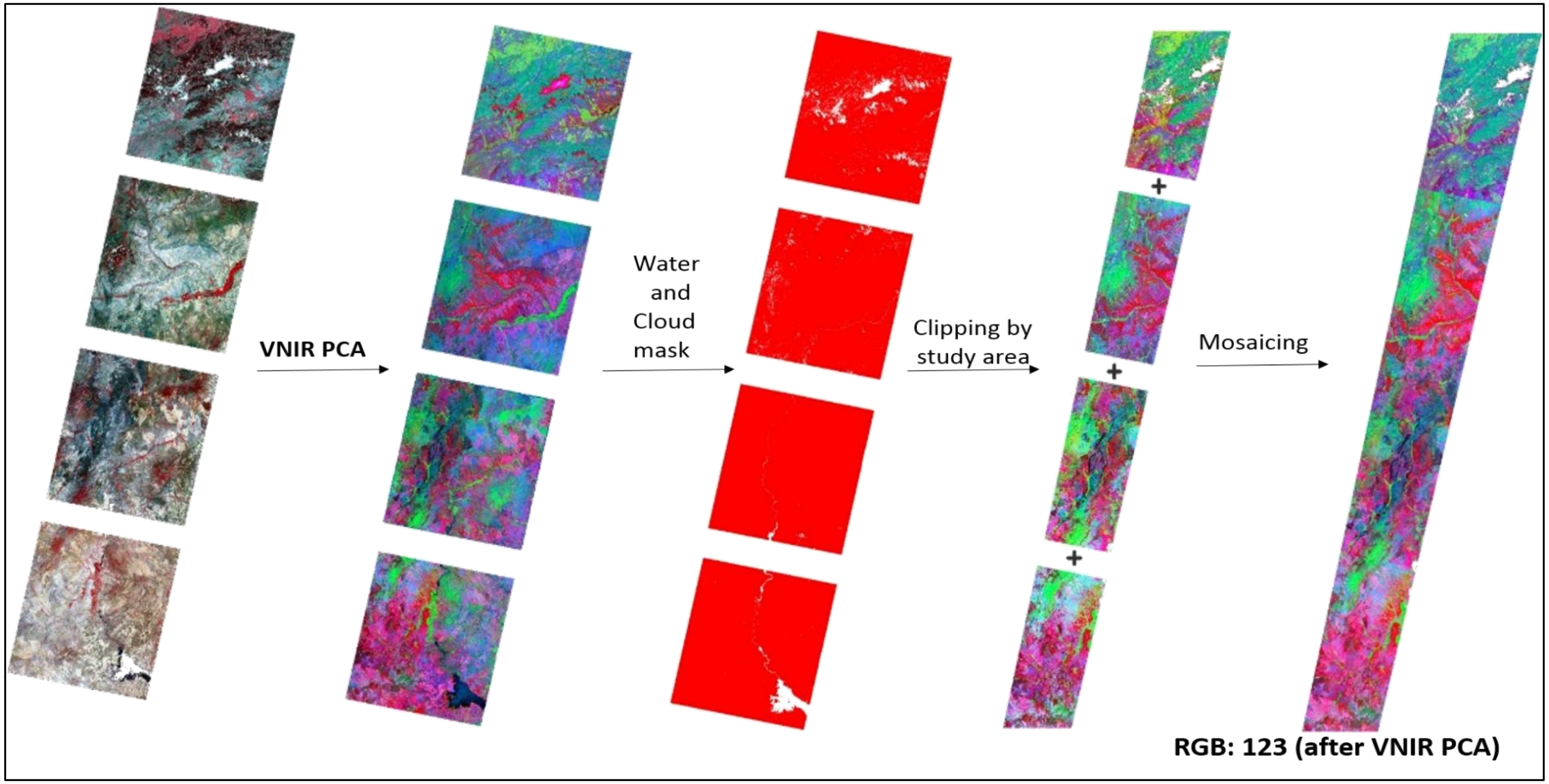

Figure 4.4. Generating Principal Component Analysis image with VNIR bands 1, 2, 3.

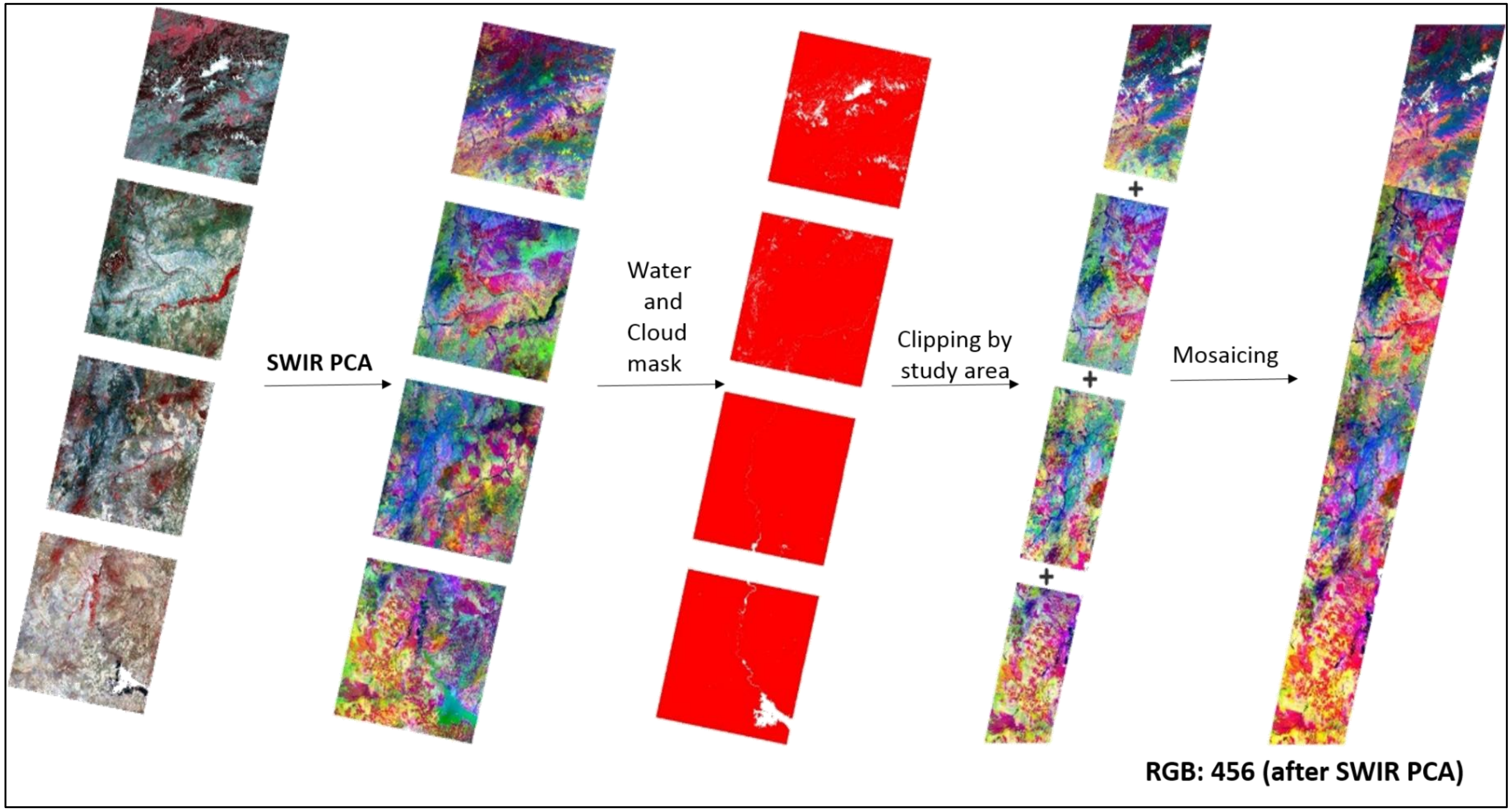

Figure 4.5. Generating Principal Component Analysis image with SWIR bands 1, 2, 3, 4, 5, 6.

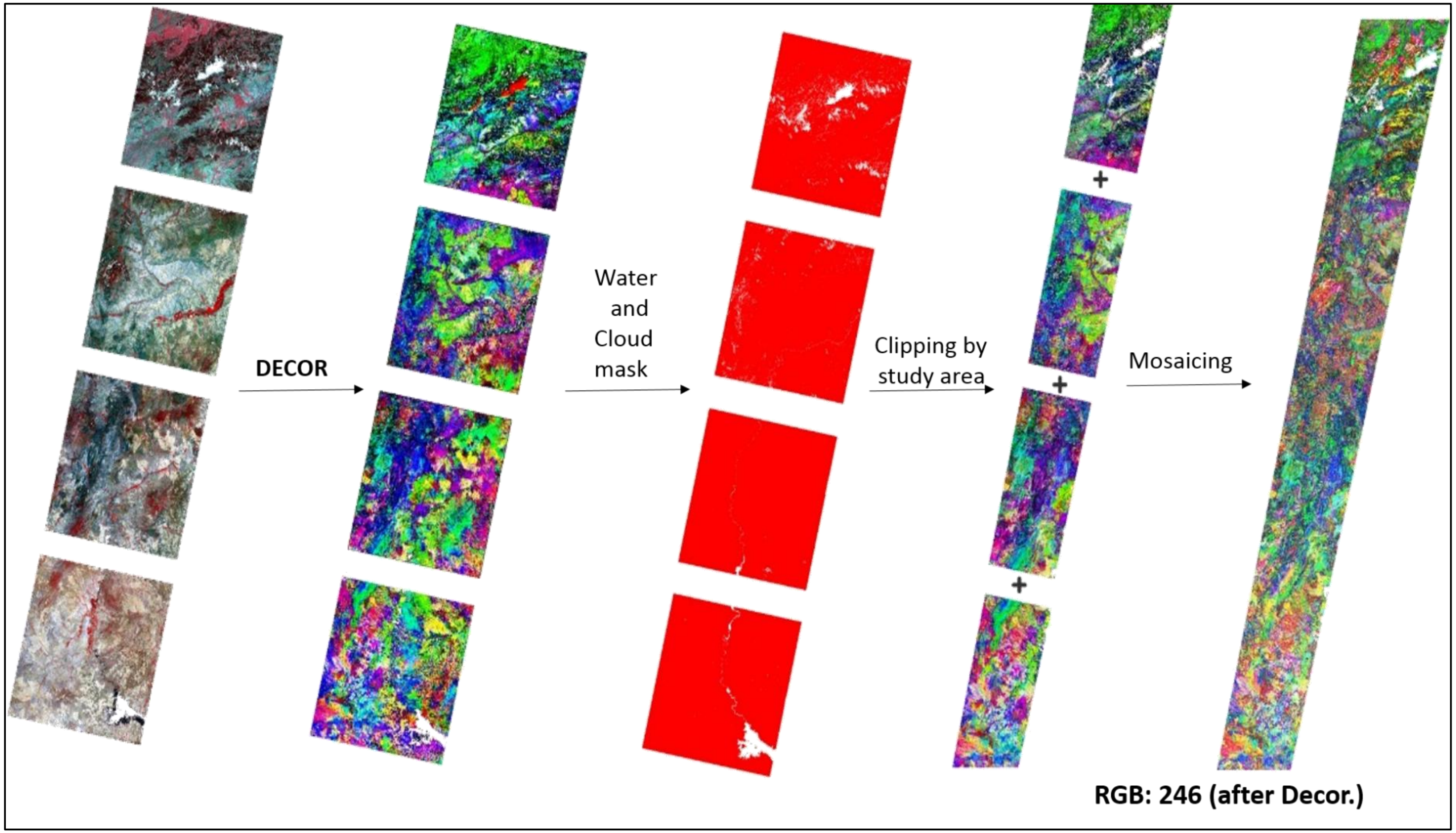

Figure 4.6. Generating decorrelation stretching image with all VNIR and SWIR bands.

CHAPTER 5

STRUCTURAL ANALYSIS

The lineaments extracted from the stereoscopic image from remote sensing data were followed and verified in the field. The spotted points were visited and the fault data were collected. In structural analysis, fault slip data were collected from the predetermined locations and this data were processed in the Win_Tensor program. After the analysis, the orientations of the stress tensors were kinematically interpreted.

5.1. Field Verification

The fieldwork was carried out in July and October 2018. In the first field study, the structural element map obtained on the basis of stereoscopic image, was confirmed by tracing the drawn lineaments in the field from North Anatolian Fault and south west of Kırıkkale. In the second field study, fault slip data were collected from the points determined with the help of aerial photographs and geological map. Strike, dip direction and angle, fault surface lineations (rake) were measured and fault types were determined. The lineaments drawn on the stereoscopic image were confirmed by tracing the major outlines in the field (Figure 5.1.).

5.2. Fault Slip Data

For the structural data collection, the fault planes and shear traces were investigated, and fault slip data were collected from 7 locations to analyze kinematically and to do kinematic interpretation (Figure 5.2.). Although the gathered slip data is not much, analyzes were still performed.

Fault plane shear data were compiled from the important points determined from the area between North Anatolian Fault and south east of Kırıkkale. The surface of the fault marked from the aerial photos could only be measured from those between the Korgun and Elmadağ. The slip data could not be detected from other spotted fault surfaces along this belt, due to weathering. The fault slip data were taken in the form of strike, dip, rake and fault sense, from pre-determined points on aerial photographs and geological map. These data were then analyzed in Win_Tensor (version 5.8.5).

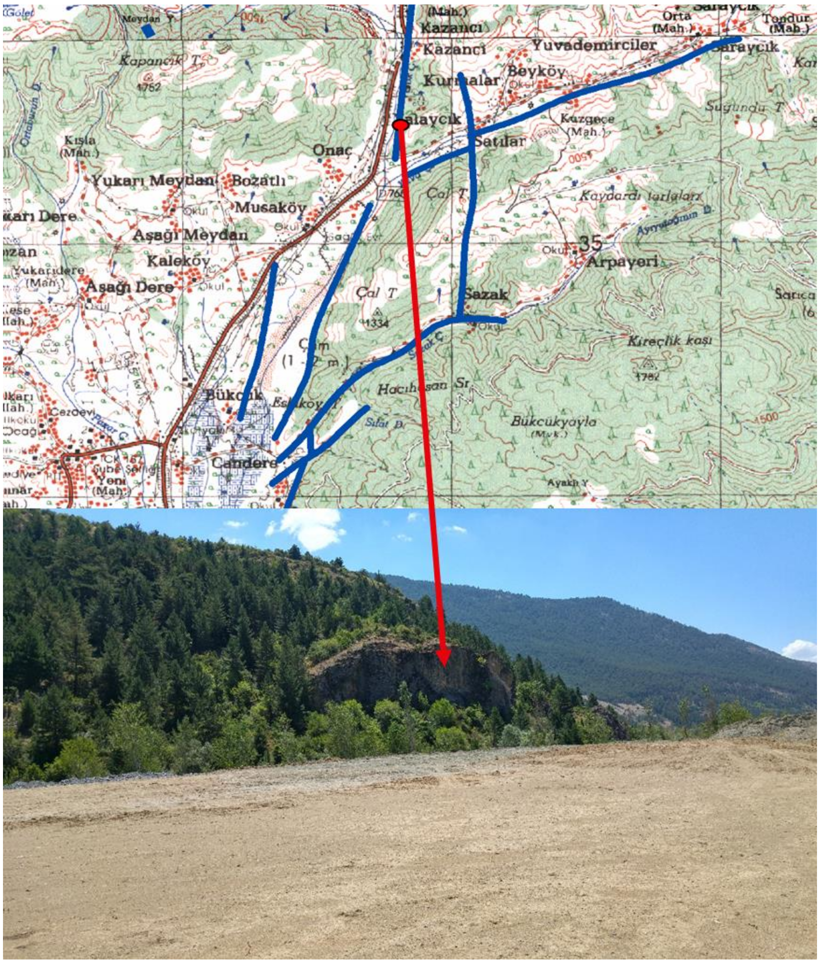

Figure 5.1. An example of the field verification study of the linear structural element map obtained from stereoscopic image (Yalaycık, Çankırı).

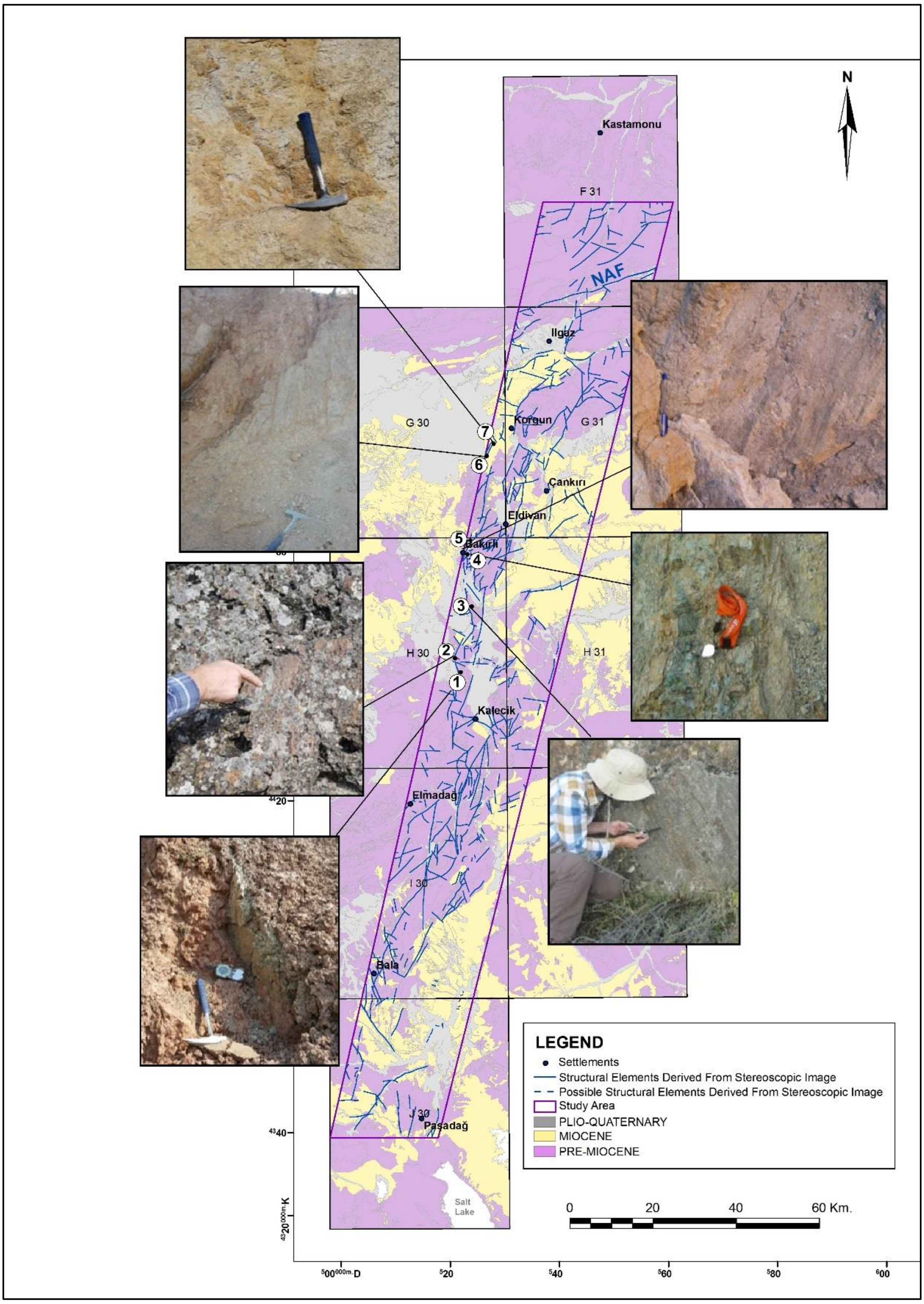

Figure 5.2. Structural elements from fault plane slip data locations in the field.

5.2.1. Win_Tensor Software

In tectonic researches, kinematic and earthquake focal mechanism analyses, fault slip data is generally used to indicate the orientation and magnitude of principal stresses. This program based on the assumption of Bott (1959), a kind of inversion method that drives the orientation of maximum shear stress from the slip of the plane. In this method, fault slip data such as strike and dip of the fault plane, orientation of the slip line and shear sense on the fault plane are used for stress tensor reconstruction. The outputs provided by this technique are maximum compression (σ_1), intermediate compression (σ_2), minimum compression (σ_3), and stress ratio (R).

Fault can be comprehended as an activated weakness plane (Delvaux and Sperner 2003). The acting stress vector σ with normal and shear stress components on the weakness plane F, has principal stress axes namely σ_l, σ_2 and σ_3, which are the largest, the intermediate and the smallest, respectively. Their states can be visualized by a stress ellipsoid (Figure 5.3.). Furthermore, their ratio $R = (\sigma_2 - \sigma_3)/(\sigma_l - \sigma_3)$ and the orientation of the fault plane states the slip direction (Angelier 1989, 1994).

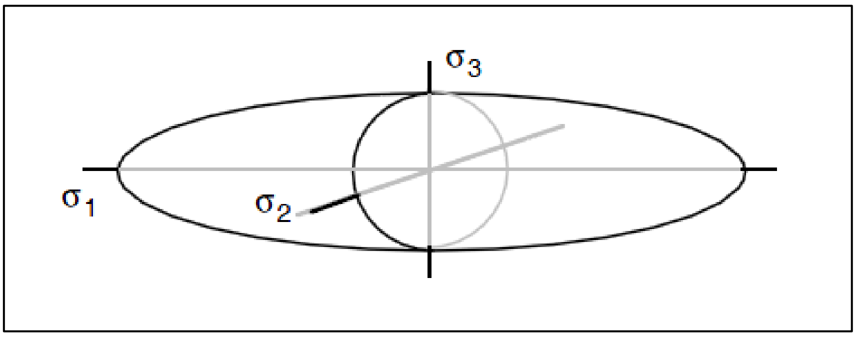

Figure 5.3. Stress ellipsoid.

Activation is related to the friction coefficient ϕ, which is calculated via normal stress component (ν) and shear stress component (τ) on the weakness plane. Friction coefficient equation is:

$$\phi = a \tan |\tau|/|\nu|$$

If friction angle ϕ exceeds the line of initial friction, weakness plane acts as fault. The behavior of the weakness plane is related to numerous vectors and other parameters, depending on the system of the stress. Vertical stress axes σ_1, σ_2, σ_3, and stress ratio R are the determiners of stress regime. Basing on σ_1 is vertical, and numeric value of R, the regimes are: $0 < R < 0.25$ (radial extension), $0.25 < R < 0.75$ (pure extension), $0.75 < R < 1$ (transtension or radial compression). Basing on σ_2 is vertical, and numeric value of R, the regimes are: $0.25 > R > 0$ (transpression), $0.75 > R > 0.25$ (pure strike slip), $1 > R > 0.75$ (transtension). Basing on σ_2 is vertical, and numeric value of R the regimes are: $0 < R < 0.25$ (transpression), $0.25 < R < 0.75$ (pure compression) (Figure 5.4.).

The orientation of σ_1 and σ_3 axes and the ratio between the principal axes (Φ) are important for the reliability of the results. Quality of the result can be accepted as good when the ratio is less than 0.4, but over 0.2. In this case, the σ_1 axis is clear. However, σ_3 axis was clear when the ratio exceeded 0.7.

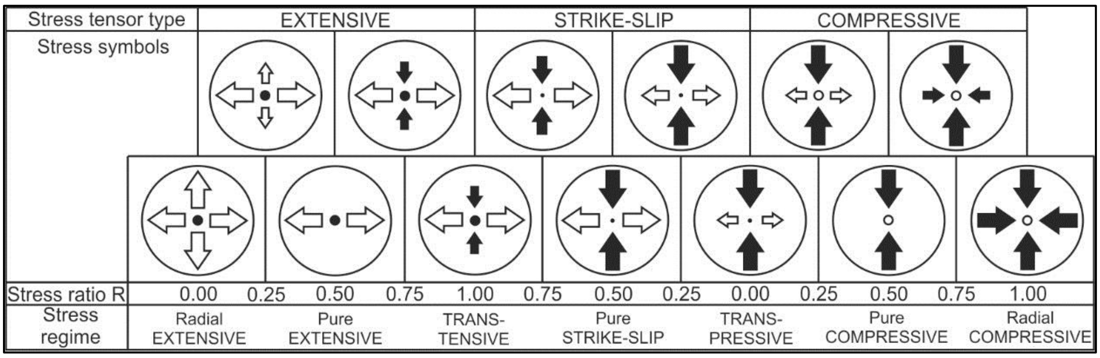

Figure 5.4. Illustration of orientation of principal axes, stress ratio R, and stress behaviours (Delvaux et al. 1997). Their length and colour symbolise the horizontal deviatoric stress magnitude, relative to the isotropic stress (σ_i). White outward arrows: extensional deviatoric stress <σ_j). Black inwards arrows: compressional deviatoric stress (>σ_i). The vertical stress (σ_v) is symbolised by a solid circle for extensional regimes ($\sigma_1 = \sigma_v$), a dot for strike-slip regimes ($\sigma_2 = \sigma_v$) or an open circle for compressional regimes ($\sigma_3 = \sigma_v$).

5.2.2. Interpretations

In the study 40 fault slip data were collected from 7 locations with their UTM coordinates and site location names. They were analyzed based on the inversion model of Angelier (Angelier 1994). Stress tensor calculations were interpreted according to table of Delvaux et al 1997 (Figure 5.4.).

Location 1: E: 530576 **N:** 4450522**,** NE of the Karahöyük Village of Kalecik

5 fault slip data were collected from fault planes which is from Miocene mudrocks-Cretaceous ophiolitic mélange contact (Figure 5.5.).

Majority of the groove directions gave normal faulting sense. After calculation of slip data in Win_Tensor program, according to the extensional deviatoric stress symbol and the stress ratio R=0.25, this location demonstrates an ESE-WNW extension (Figure 5.6.).

Location 2: E: 529349 **N:** 4453676**,** Değirmenkaya Village of Kalecik

5 fault slip data were conducted from Miocene-melange contact in neotectonic fault zone. In this location there are also small faults which were observed in melange.

After calculation of slip data in Win_Tensor program, according to the compressional deviatoric stress symbol and the stress ratio R=0.67, this location demonstrates a NE-SW compression (Figure 5.7.).

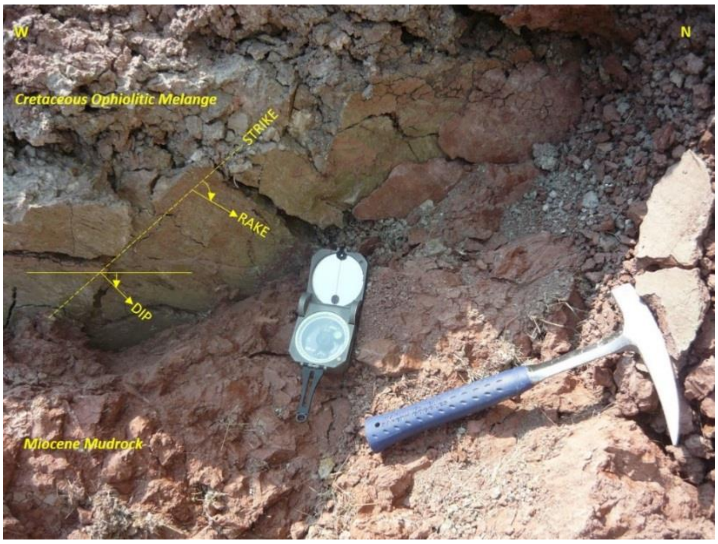

Figure 5.5. Miocene mudrocks-Cretaceous ophiolitic Melange contact from the NE slope of Karahöyük Village (GPS Location: 530576 E, 4450522 N).

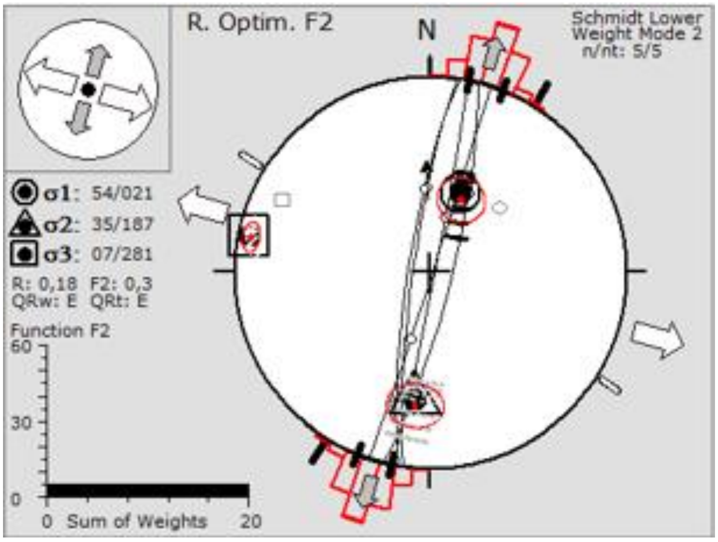

Figure 5.6. Win_Tensor data worksheet for location 1 (GPS Location 530576 E, 4450522 N).

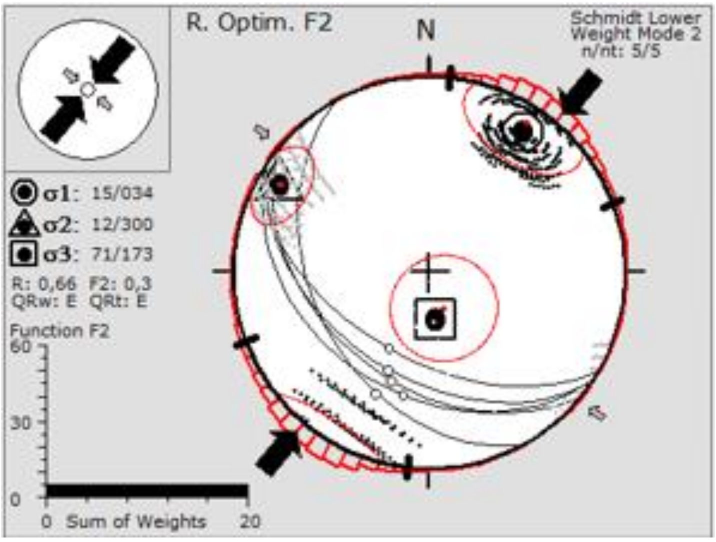

Figure 5.7. Win_Tensor data worksheet for location 2 (GPS Location: 529349 E, 4453676 N).

Location 3, E: 533394 **N:** 4466275**,** Karatepe Village of Kalecik

5 fault slip data were collected from a fault developed between Jurassic carbonates and Miocene mudrocks (Figure 5.8).

At close up, the scaly matrix increased, and the stratification get lost. Majority groove directions manifest normal faulting. After the analysis of the slip data in Win_Tensor program, according to the extensional deviatoric stress symbol and the stress ratio R=0.39, this location demonstrates an almost N-S extension (Figure 5.9.).

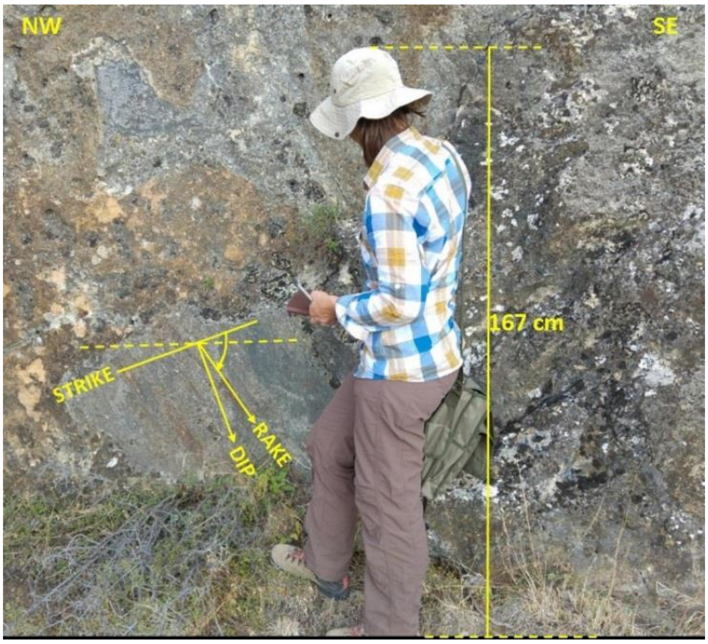

Figure 5.8. Measurement from the fault plane, location 3 (GPS Location: 533394 E, 4466275 N).

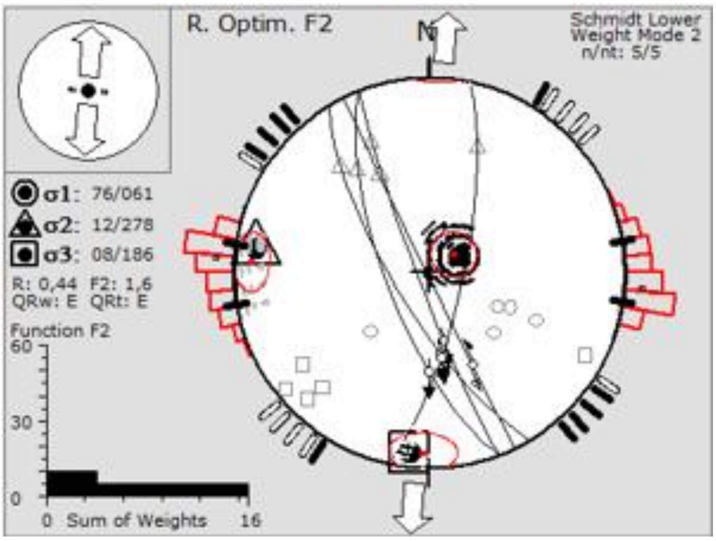

Figure 5.9. Win_Tensor data worksheet for location 3 (GPS Location: 3533394 E, 4466275 N).

Location 4: E: 532262 **N:** 4479658, Bakırlı Village of Şabanözü

2 fault slip data were conducted along the fault zone which was developed along the components of Cretaceous ophiolitic mélange. Any link with the Miocene sequences could not be seen (Figure 5.10.).

After the analysis of the slip data in Win_Tensor program, according to the compressional deviatoric stress symbol and the stress ratio R=0.50, this location demonstrates a NE-SW compression (Figure 5.11.). However, age relationship cannot be identified due to the fault solely confined to the Cretaceous mélange. High silicification and intense shearing was observed along the mineralized fault zone (Fig. 5.10.).

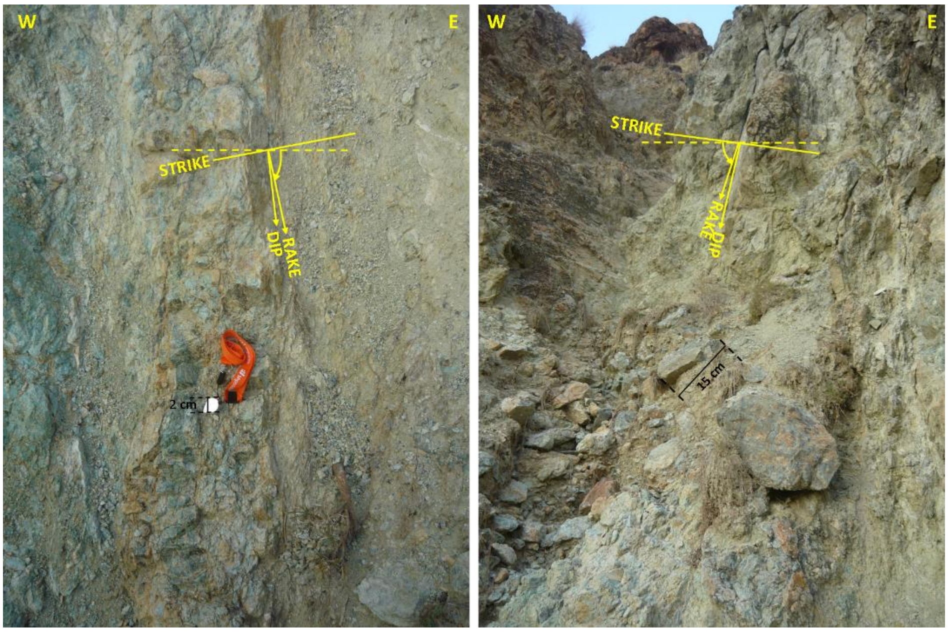

Figure 5.10. Shear plane in Bakırlı Village, location 4 (GPS Location: 532262E, 4479658N).

Location 5: E: 532325 **N:** 4479675**,** Bakırlı Village of Şabanözü

13 fault slip data were conducted from fault with silicified and altered serpentinite (Figure 5.12.). After calculation of slip data in Win_Tensor program, according to the compressional vertical deviatoric stress symbol and the stress ratio R=0.65, this

location demonstrates NNE-SSW compression (Figure 5.13.). The analyzed data manifest a reverse fault with sinistral components.

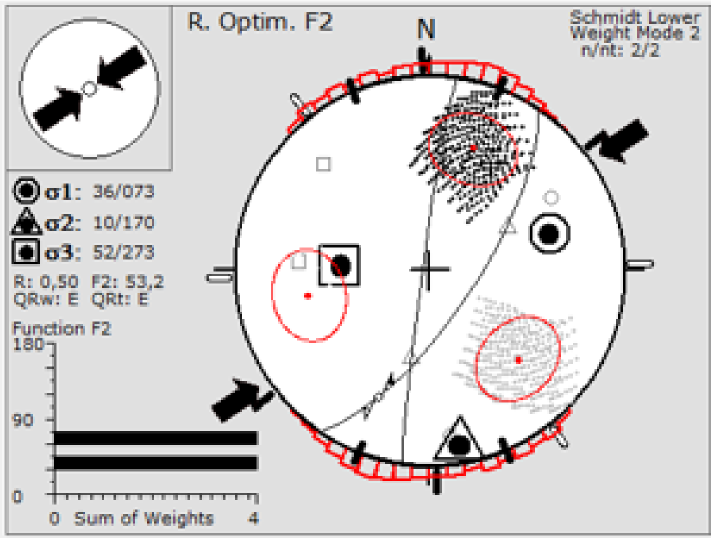

Figure 5.11. Win_Tensor data worksheet for location 4 (GPS Location: 532262 E, 4479658 N).

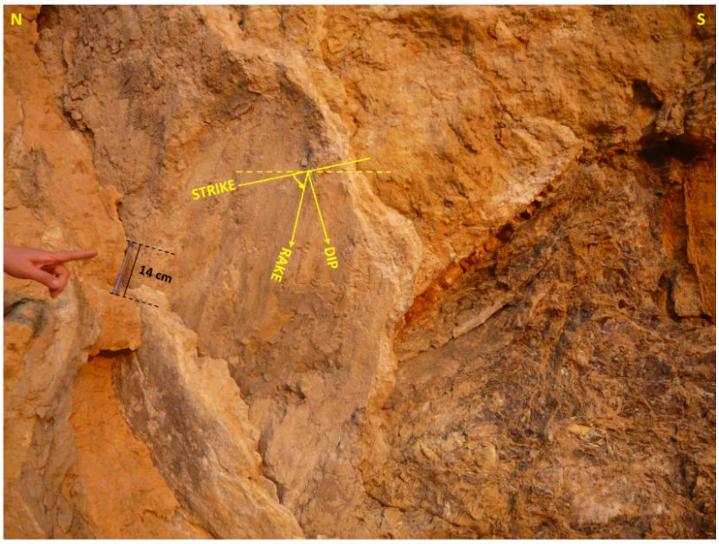

Figure 5.12. Fault slip lines on tuff, location 5 (GPS Location: 532325 N: 4479675 E).

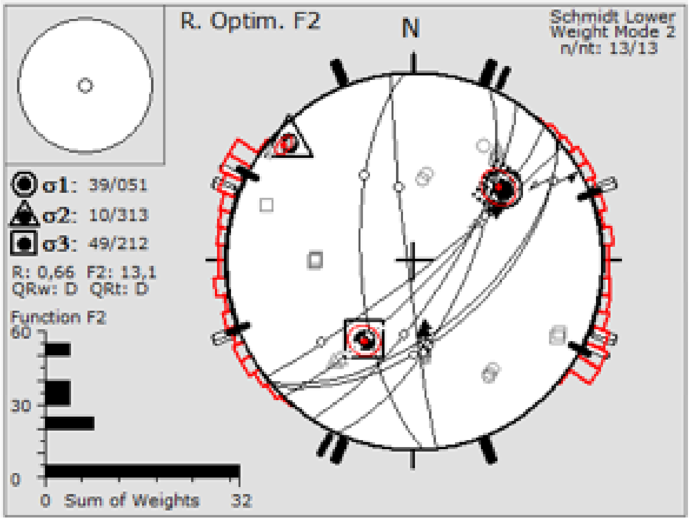

Figure 5.13. Win_Tensor data worksheet for location 5 (GPS Location: 532325 N: 4479675 E).

Location 6: E: 536993 **N:** 4502412, SW of Yolkaya Village of Korgun

8 fault slip data were collected from Miocene tuffs. There are secondary slip data overprinted onto the other sets (Figure 5.14.).

After the analysis of the slip data in Win_Tensor program, according to the extensional deviatoric stress symbol and the stress ratio R=0.42, this location demonstrates WNW-ESE extension (Figure 5.15.).

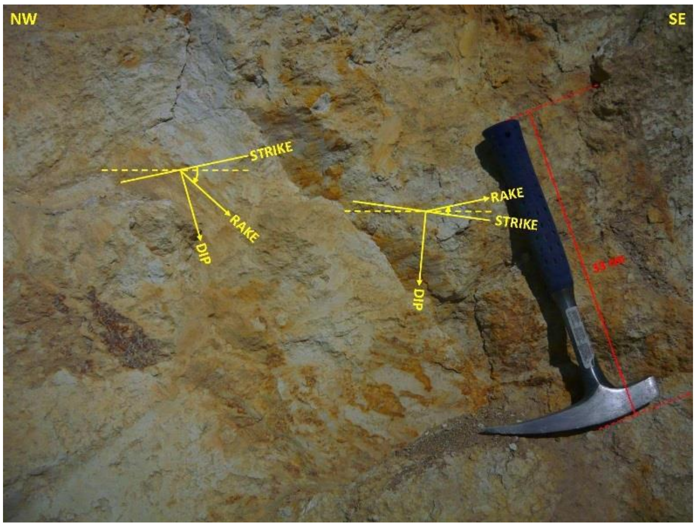

Figure 5.14. Shears on tuff on Kayıçivi-Yolkaya Road, location 6 (GPS Location: 536993 E, 4502412 N).

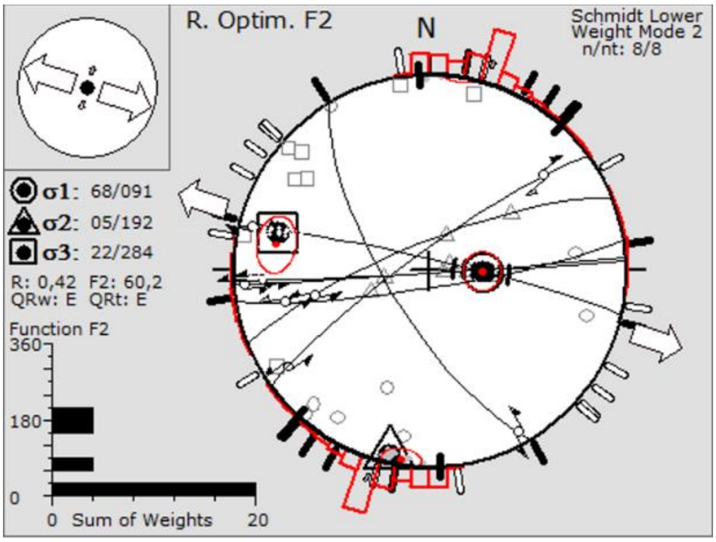

Figure 5.15. Win_Tensor data worksheet for location 6 (GPS Location: 532262 E, 4479658 N).

Location 7: E: 538531 **N:** 4505475, Kayıçivi Village-SW of Korgun

2 fault slip data were collected from a fault developed in Miocene volcanic-sequences with a 1m post-Miocene fill. The fill is composed of poorly sorted, brown-red breccias with occasionally recorded volcanic and metamorphic rock fragments (Figure 5.16.). Majority groove directions manifest normal faulting.

After the analysis of the slip data in Win_Tensor program, according to the stress orientations and the stress ratio is near R=1, this location demonstrates a WNW-ESE transtension with dominant WNW-ESE extension and NW-SE sinistral strike slip component (Figure 5.17.).

Overview of the stereograms and photos of the locations were shown on simplified geological map (Figure 5.18.).

To summarize, stress tensor calculations were interpreted according to Delvaux et al. 1997, with 40 fault slip lines from 7 locations.

Figure 5.16. A meter thick fill along a fault at Korgun-Kayıçivi, location 7 (GPS Location: 538531 E, 4505475N).

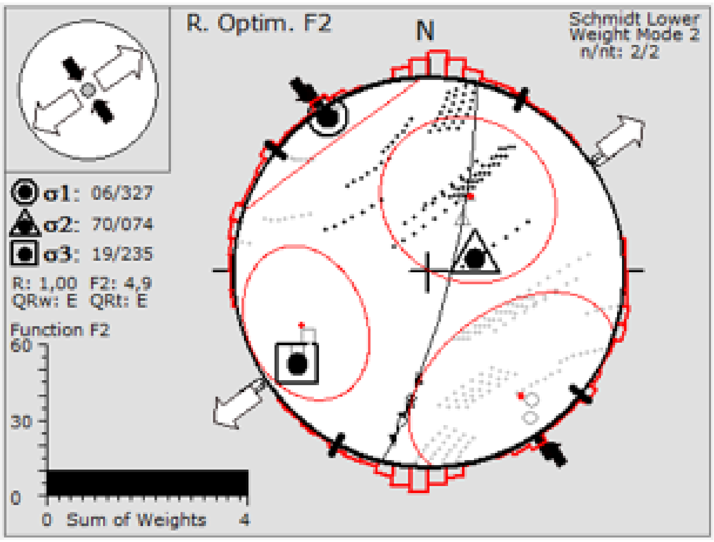

Figure 5.17. Win_Tensor data worksheet for location 7 (GPS Location: 538531 E, 4505475 N).

The fault slip data manifests various kinematic results. However, the slip data from the faults cross-cutting the Cretaceous ophiolitic melange reveals a NE-SW compression. When the fault slip data collected from the faults cross-cutting, the Miocene sequences reveals a kinematic result of an extension orientation changing from E-W to NNE-SSW directions.

There were more than seven locations and post-Miocene (neotectonic) faults recorded from remote sensing data, in the field. However, fault slip data could not be collected due to weathering, vegetation etc. As an example of the neotectonic faults, on the Kayıçivi-Çukurören road, two different types of agglomerates, coarse pyroclastics on the east and tuffaceous material on the west, and a west dipping normal fault were observed (Figure 5.19.).

Since the subject of the study that is the neotectonic period, the faults, which are identified on stereoscopic images that correspond to the units belonging to Miocene and post-Miocene periods on the geology map, were confirmed with field observations. The cut surfaces in the Miocene on the road from Koyunbaba to Şemsettin Villages in Kalecik district are examples of this kind of observations (Figure 5.20.). However, no fault slip data were observed.

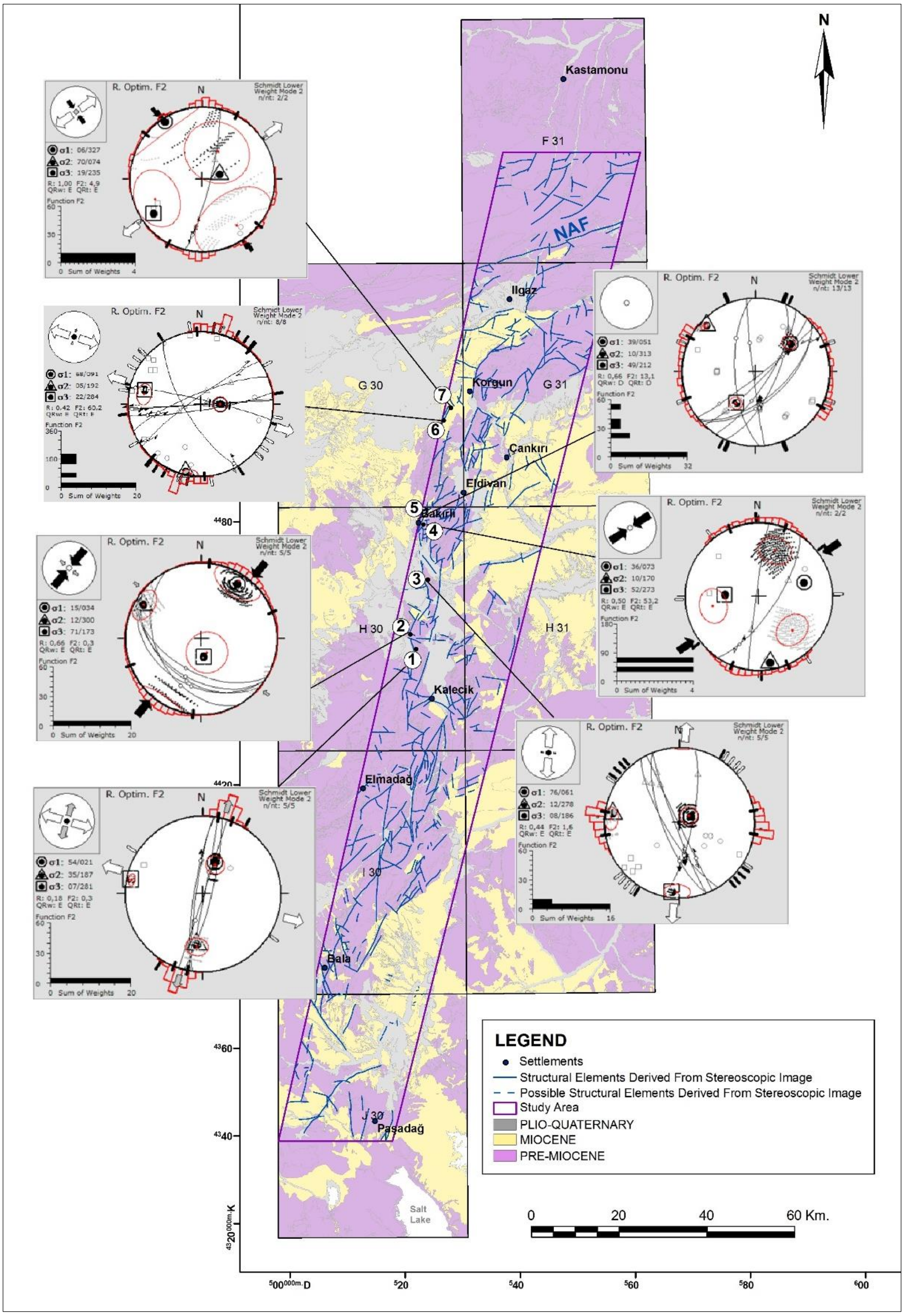

Figure 5.18. Overview of the stereograms and photos of the locations are shown on simplified geological map (NAF; North Anatolian Fault).

Figure 5.19. Normal fault with, coarse pyroclastics on the left and tuffaceous west dipping falling block on the right.

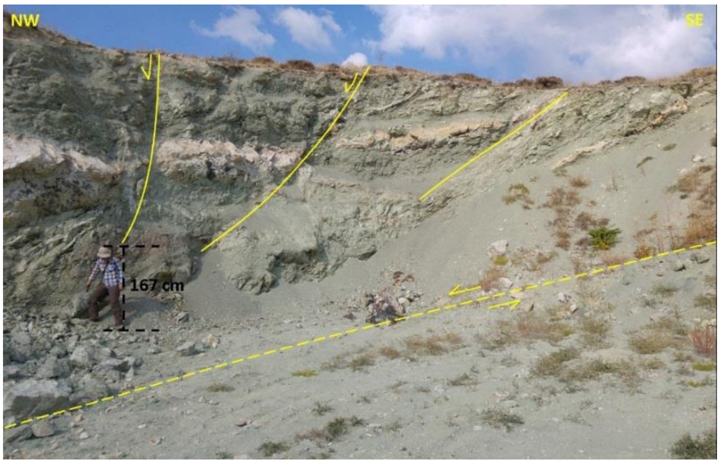

Figure 5.20. Shear planes in Miocene on the right side of the road from Koyunbaba to Şemsettin Village (GPS Location: 527056 E, 4462629 N).

CHAPTER 6

DISCUSSION

For the NW Central Anatolia, Koçyiğit (1991), Koçyiğit et al. (1995) offer a NW-SE compressional regime due to collisional tectonics continued until pre-Late Miocene and N-S compressional regime due to strike slip faults keep on until late early Pliocene. This is based on the thrusting of the ophiolitic units onto Neogene (Pliocene) units (Koçyiğit 1991). On the other hand, this thesis stands up for NE-SW compressional NNW-SSE strike slip faulting developed before normal faulting during post-Pliocene and no observation for thrust fault in Plio-Quaternary.

On the other hand, Seyitoğlu et al. (1997) claims that there is no thrusting but strike slip faulting between basement and Miocene succession from detailed search on slickensides and no enough data for compressional regime during Miocene-Late Pliocene. He states that the compressional regime ended after Oligocene-or earliest Miocene, and extensional regime improved during middle to late Miocene probably because of gravitational collapse and transpression or transtension of NAF. In this study, the transtensional stress regime solution, might be interpreted as resulted from post-Miocene transtensional regime in the region controlled by the NAFZ as proposed by Seyitoğlu, 1997.

Kaymakci (2000) offers that Early-Middle Miocene extensional system by orogenic collapse, and then Late Miocene-Recent transpression occcured in Çankırı region related to initiation of NAFZ. He states the western margin of Çankırı Basin as a transpressive sinistral strike-slip zone, which is Eldivan Fault Zone (EFZ). However, an extensional tectonic regime has been concluded at the stated location of the transpressional regime after the Miocene.

Rojay and Karaca 2008, in their study about tectonic evolution of Central Anatolia, comment on the activity of Central Anatolia that post-Miocene NW-SE trending compression from the bedding attitudes, E-W directed extension from the faults in Plio-Quaternary units, and post-Plio-Quaternary NW-SE to NNE-SSW multidirectional extension partly by the activity of North and East Anatolian faults and lately by the diffusion of NE-SW trending Aegean graben extension. From stress solutions in this thesis, that is, NE-SW to NW-SE extensional regime resulting a multidirectional normal faulting in post-Miocene trending NW-SE to NE-SW can be thought as a supportive result for Rojay and Karaca 2008.

In previous studies, the zone was proposed as Eldivan- Elmadağ Pinched Crustal Wedge (EPCW) by Seyitoğlu et al. 2009 and Eldivan Fault Zone (EFZ) by Kaymakçı 2000. This fault zone was also detected by lineament analysis and confirmed by slip data in this thesis.

In this study, different stress regimes were observed between pre-Miocene and post-Miocene, that is Pre-Miocene compressional and post-Miocene extensional regimes with fieldwork and stress analyses. An NE-SW extensional regime resulting a multidirectional normal faulting in post-Miocene trending NW-SE to NE-SW, and NE-SW compressional NNW-SSE strike slip faulting developed before normal faulting (Figure 6.1.). In the northermost area which was the slip data taken, namely location 7, gives transtensional stress regime solution, may be interpreted as resulted by post-Miocene transtensional regime in the region controlled by the NAFZ. Further south, this effect is reduced and replaced by a compressional regime in pre-Miocene and an extensional regime in post-Miocene. NE-SW pre-Miocene compressional regime can be interpreted as controlled by intercontinental convergence. Besides, the multi-directional extension in post-Miocene trending NW-SE to NE-SW can be thought as the continuation of the NE-SW trending Aegean graben.

Structural element map was extracted from stereoscopic image by remote sensing studies. 3-dimensional image of the topography was obtained with this technique. In

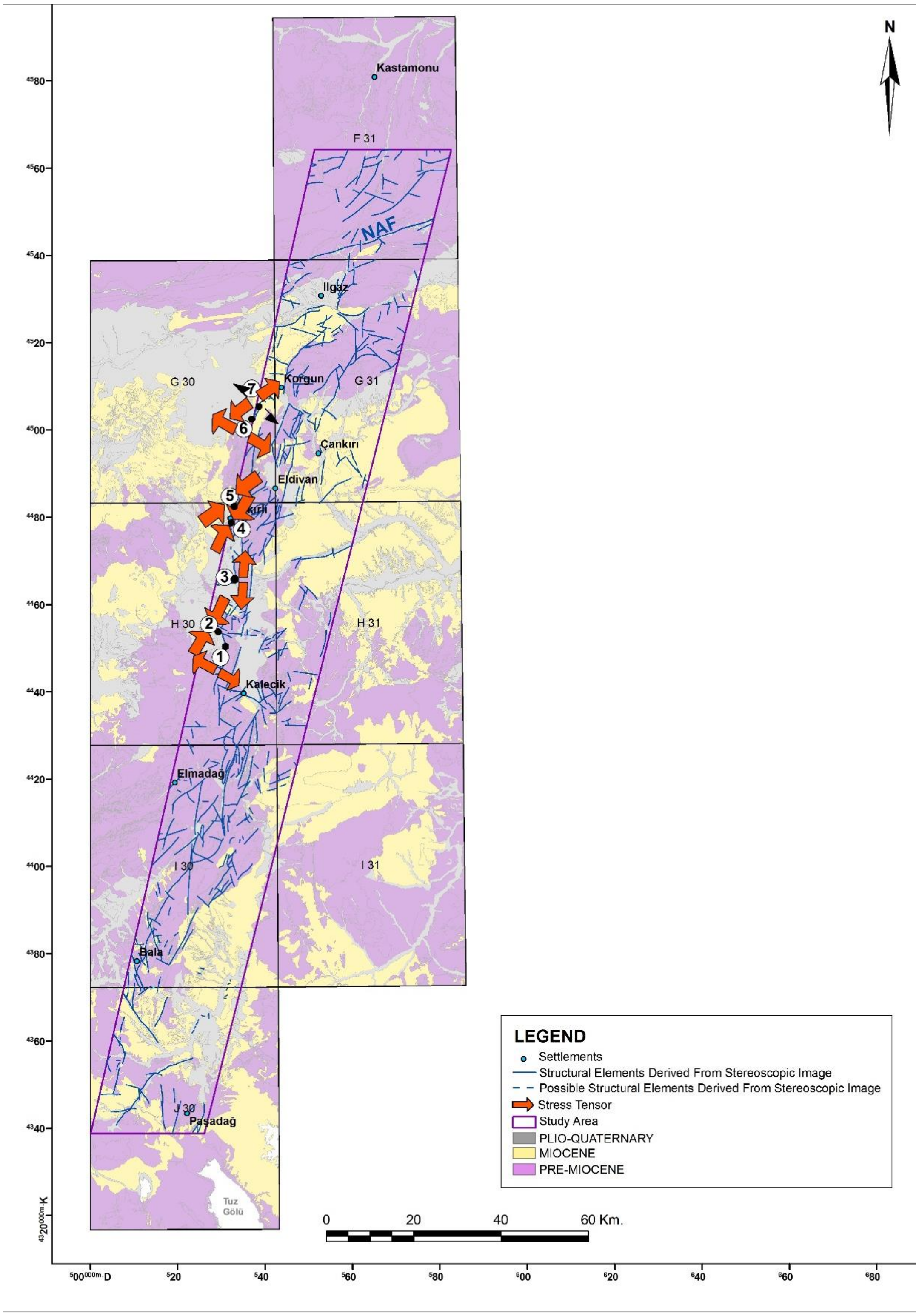

Figure 6.1. Kinematic interpretation of fault slip data on structural element map derived from stereoscopic image.

this way, topographical discontinuities and linear structures were easily detected by the perception of being in the field. Shaded relief map extraction with DEM as a GIS technique has the same function and it was used as an auxiliary layer in lineament analysis. The structural element map was created over stereoscopic image obtained from Terra ASTER images also overlapped with shaded relief map produced by GIS studies. Similarly, it was concluded that it is also available to be used as a control layer for structural element map (Figure 6.2.).

Principal Component Analysis and Decoration Stretching, which are the image enhancement techniques in remote sensing studies, were applied for the detection of lithological structural discontinuities by emphasizing lithological differences and used as control layers. VNIR PCA in RGB: 123, SWIR PCA in RGB: 456 and decorrelation image in RGB: 246 maps were overlapped individually by structural element map created from stereoscopic image (Figures 6.3., 6.4., and 6.5. respectively). As the color contrast increases by PCA and decorrelation methods, it provides a wider range of information on the RGB color scale, allowing the eye to perceive lithological differences more easily. According to results, PCA and decorrelation stretch methods were approved to be available to emphasize the lithological differences to find out the possible structural elements that can be originated from these differences. Thus they can be used as auxiliary materials to create lineament maps. Here, needing to pay attention that non-structural lineaments can be confused with structural lineaments, as each lithological boundary does not imply a structural lineament, such as tilted bedding planes etc.

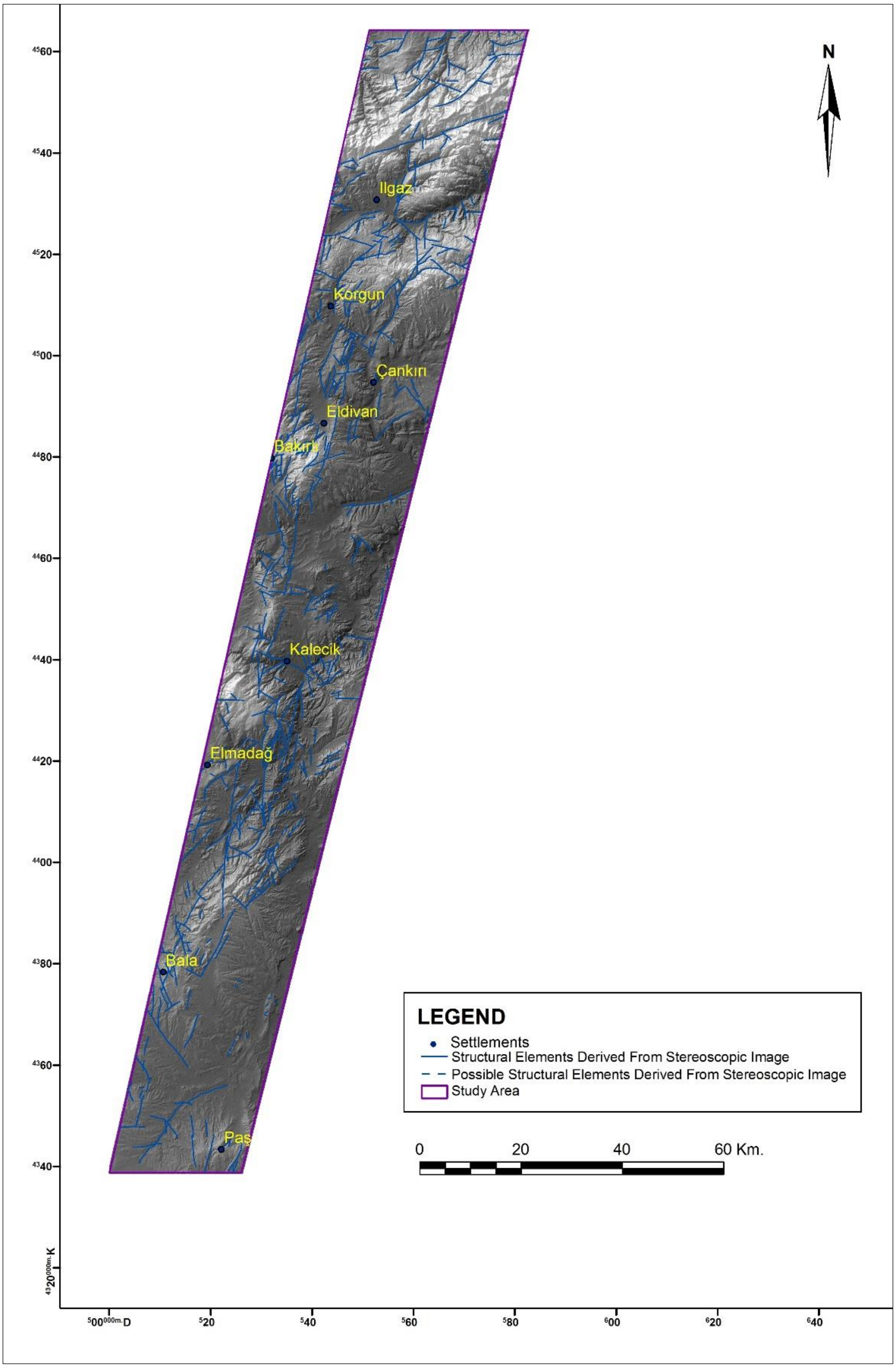

Figure 6.2. Shaded relief image and structural element map derived from stereoscopic image.

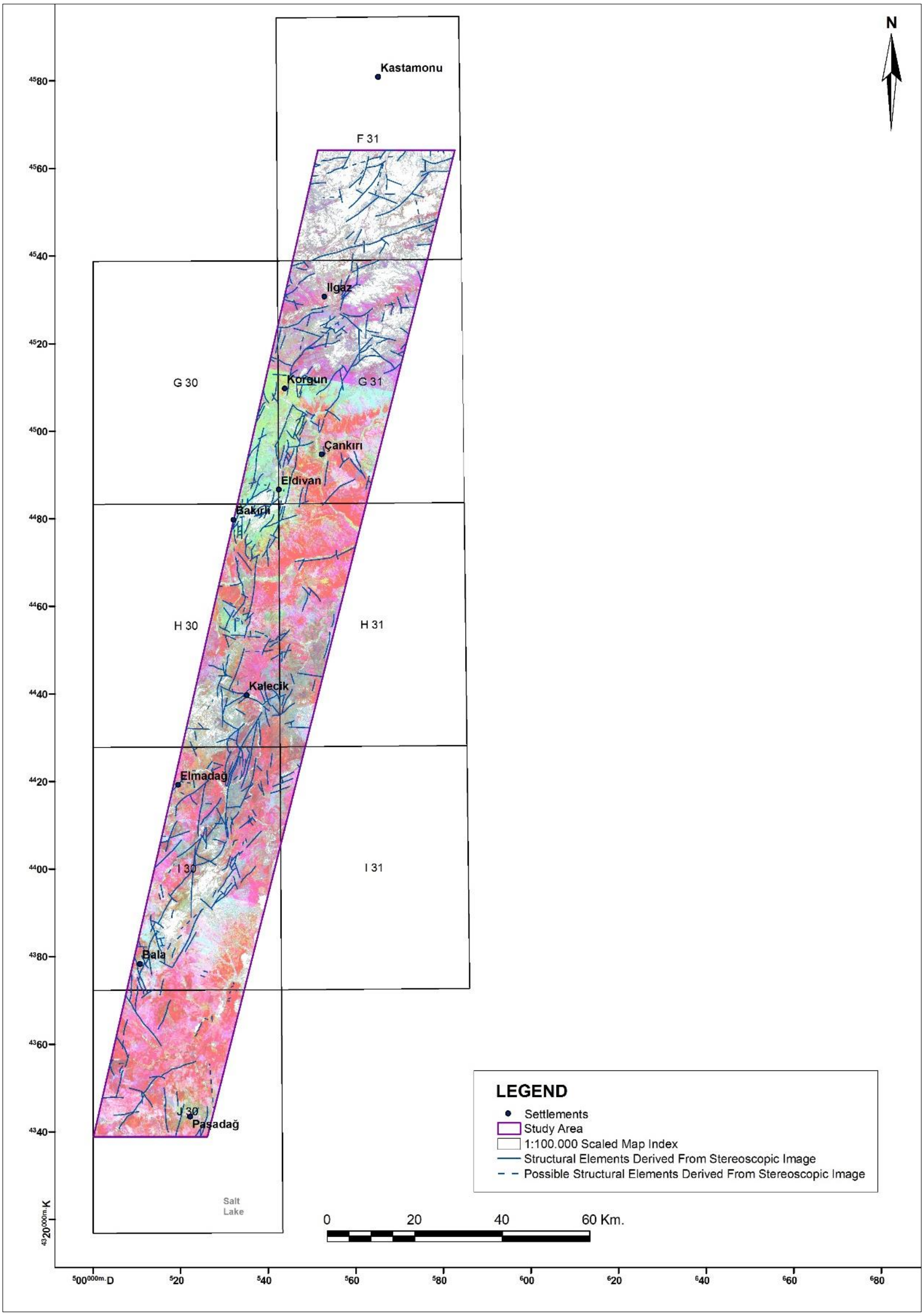

Figure 6.3. VNIR PCA image and structural element map derived from stereoscopic image.

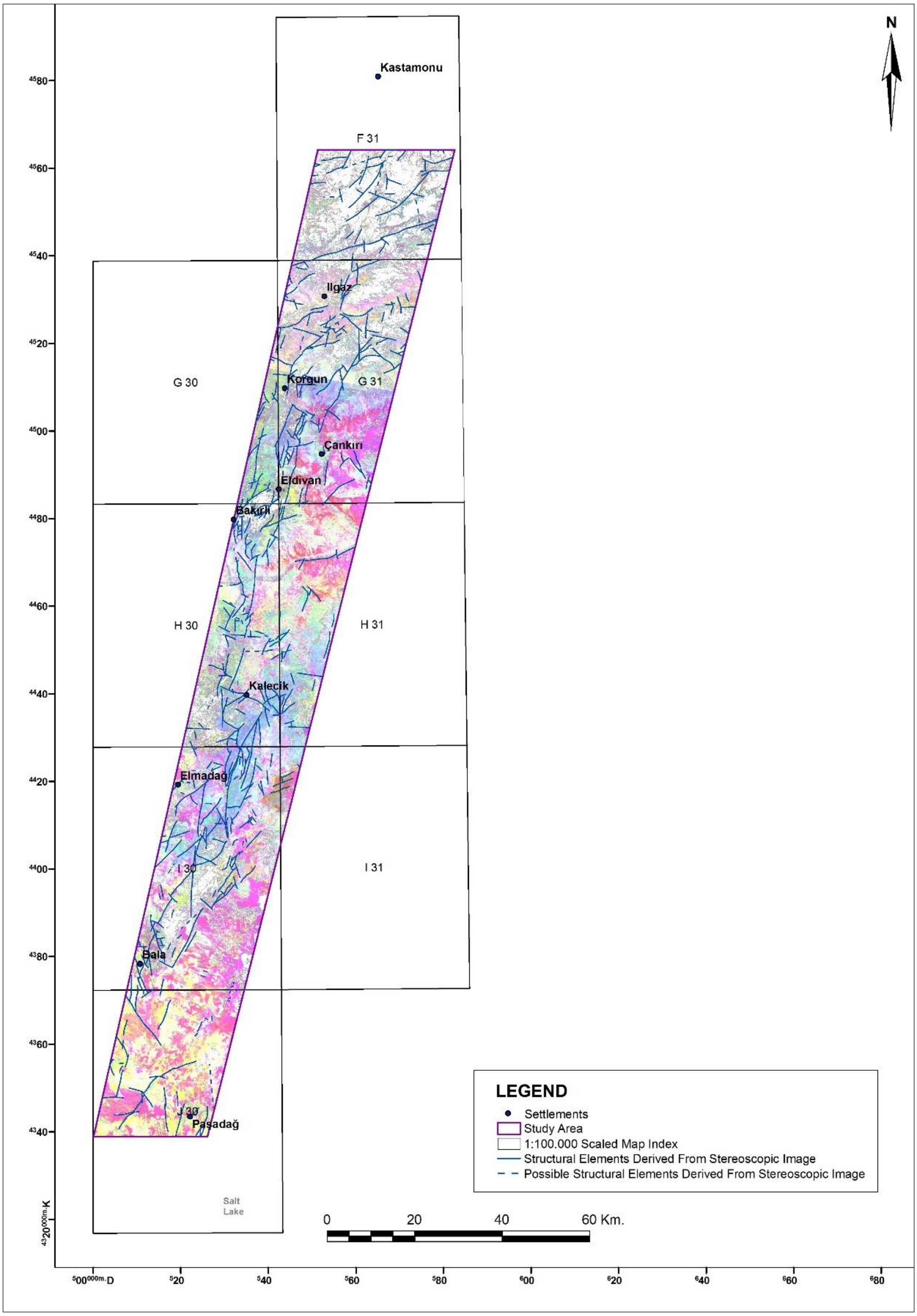

Figure 6.4. SWIR PCA image and structural element map derived from stereoscopic image.

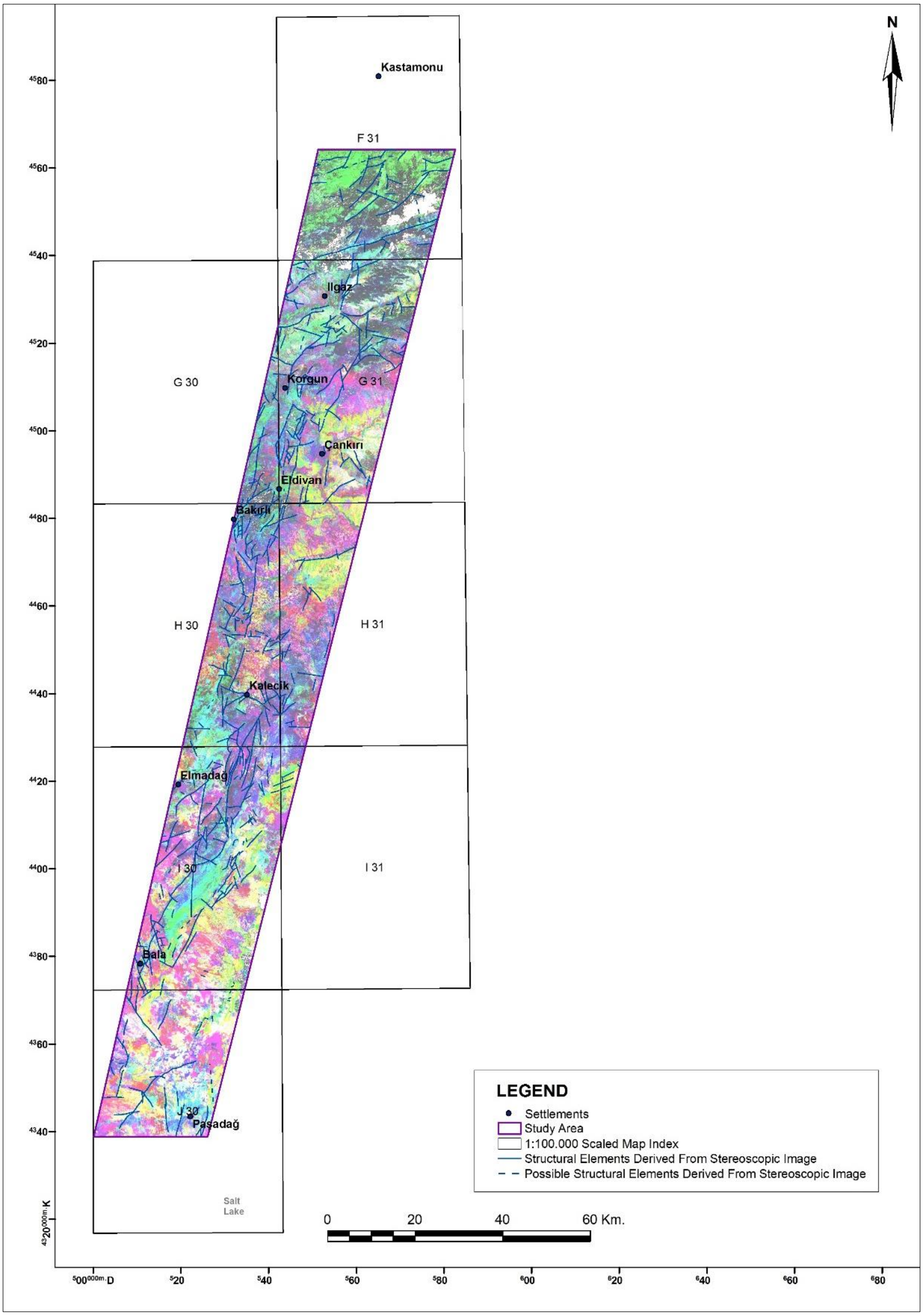

Figure 6.5. Decorrelation stretching image and structural element map derived from stereoscopic image.

CHAPTER 7

CONCLUSIONS

In this research, remote sensing studies were executed for structural element mapping, enabling the advantages of remote sensing in economic, time, extent, spectral, and remote accessibility. NNE-SSW general trending lineament was visualized by length weighted rose diagram, between NAFZ and TGF, with the data gathered from the remotely sensed images. The aim of the length weighted plot was to detect the predominant deformation. According to the data obtained from the satellite images by remote sensing methods, NNE-SSW trending length weighted lineament is linking NAFZ in the north to TGF in the south (Figures 7.1. a. and b.).

Additionally, a non-weighted rose diagram was plotted for the same data gathered from the remotely sensed images (Figure 7.1. c.). NNE-SSW trending lineament was resulted according to non-weighted diagram, which has a more or less familiar trend with the length weighted diagram. The fact that short lineaments detected by non-weighted rose give close results to the main deformation trend determined by length-weighted, led us to conclude that the stress regime causes similar trends in deformation in large and small structures.

The fault slip data were compiled from the area between NAF and TGF. The collected fault slip data were analyzed in Win_Tensor (version 5.8.5) program. According to the fault slip data collected on the faults and paleostress analysis, two groups of fault were recognized. The first group has NE-SW to NW-SE extensional regimes, resulting NW-SE to NE-SW trending normal movement. These faults intersect the Miocene units and thus, their age is probably after Miocene. Other group of faults has NE-SW compressional NNW-SSE trending strike slip faults and it is commented that it developed before normal faulting due to cross cutting relations.

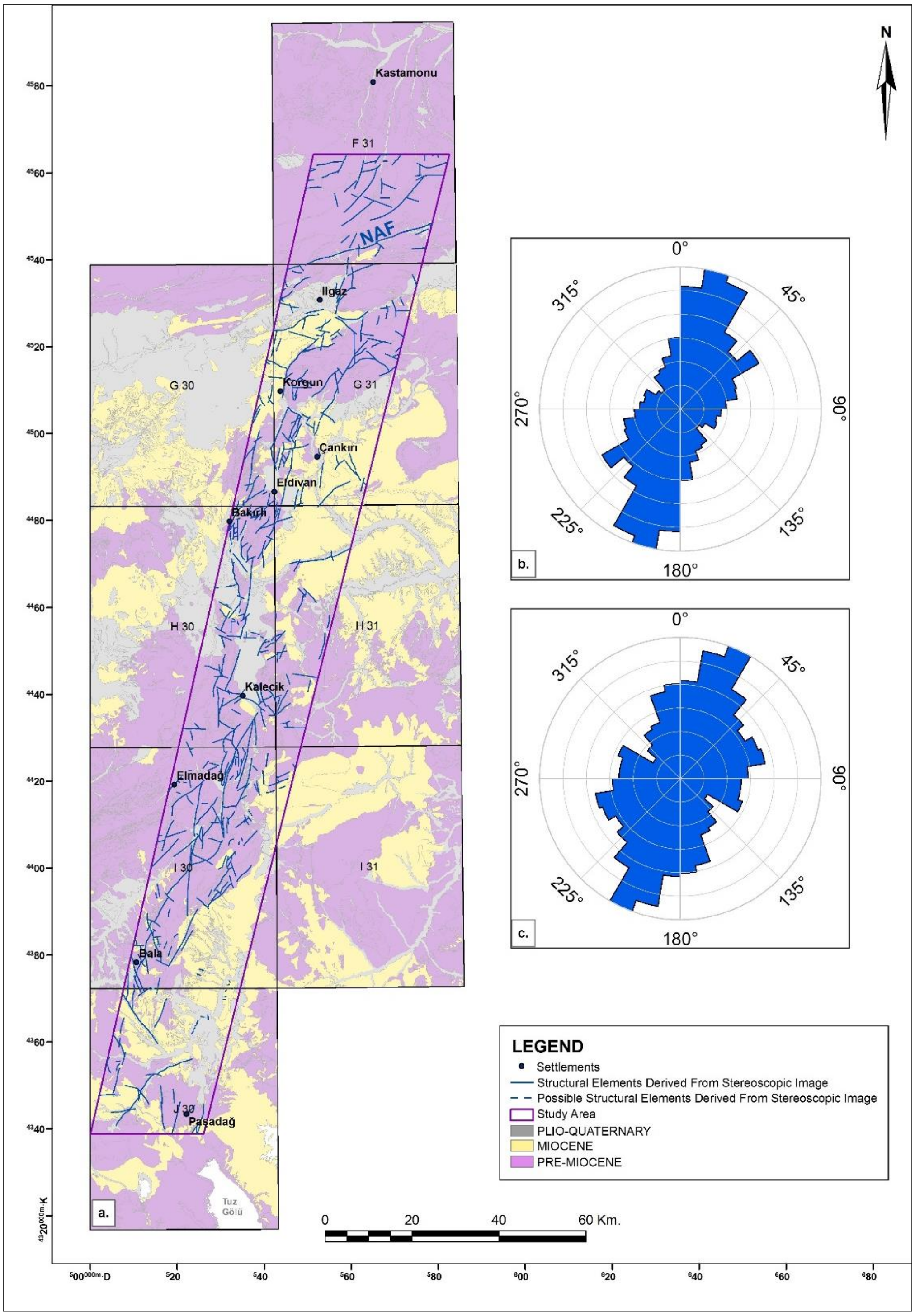

Figure 7.1. a. Structural element map derived from stereoscopic image, b. Length weighted rose diagram of the lineaments on map a, c. Non-weighted weighted rose diagram of the lineaments on map a.

i) The lineament analysis done on the weighed rose diagram of the lineaments point out a NNE-SSW trending lineament zone which is probably the fault zone orientation.

ii) There is more or less a familiar trend comparing the length weighted and non-weighted rose diagrams of the structural element map derived from stereoscopic image. Similar deformational orientation was observed at different length of structures under the same stress regime.

iii) The spotted points on the lineaments -faults-, especially the ones spotted by aerial photographs, were visited to collect fault slip data. In seven locations fault slip data were collected.

iv) The fault slip data manifests various kinematic results. However, the slip data from the faults cross-cutting the Cretaceous ophiolitic melange reveals a NE-SW compression. The fault slip data collected from the faults cross-cutting the Miocene sequences reveal a kinematic result of a multiextensional terrain evolution from E-W to NNE-SSW directions.

REFERENCES

Agusti, J., Cabrera, L., Garces, M., Krijgsman, W., Oms, O., and Pares, J.M., 2001. A calibrated mammal scale for the Neogene of Western Europe: State of the art. Earth-Science Reviews 52, pp. 247–260.

Akçay, A.E., Dönmez, M., Kara, H., Yergök, F.A. ve Esentürk, K., 2008. 1:100 000 ölçekli açınsama nitelikli Türkiye Jeoloji Haritaları serisi, Kırşehir-J30 paftası, No:91. Maden Tetkik ve Arama Genel Müdürlüğü, Ankara.

Akyol, E., 1968. Ankara-Kızılcahamam, Çeltikçi Civarında Bulunan Kömür Zuhurlarının 1/25000 Ölçekli Detay Jeolojik Etüdü Hakkında Rapor. Maden Tetkik Arama Enstitüsü report no. 4405.

Akyürek, B., Bilginer, E., Akbaş, B., Hepşen, N., Pehlivan, Ş., Sunu, O., Soysal, Y., Dağer, Z., Çatal, E., Sözeri, B., Yıldırım, H. ve Hakyemez, Y., 1984. Ankara-Elmadağ-Kalecik dolaylarının jeolojisi. Jeoloji Mühendisliği Dergisi 20, pp. 31-46.

Angelier, J., 1989. From orientation to magnitudes in paleostress determinations using fault slip data. Journal of Structural Geology, 11, pp. 37-50.

Angelier, J., 1994. Fault slip analysis and paleostress reconstruction. In: Hancock, P. L. (ed.) Continental Deformation. Pergamon, Oxford, pp. 101-120.

ASTER Users Handbook, Abrams, M., Hook, S., 2002. Jet Propulsion Laboratory California Institute of Technology, Version 2, p. 135.

Bott, M.H.P., 1959. The mechanics of oblique slip faulting. Geological Magazine, 96, pp. 109-117.

Burrough, P.A., and McDonell, R.A., 1998. Principles of Geographical Information Systems (Oxford University Press, New York), p. 190.

Chavez, Jr, P.S., 1996, Image-based atmospheric corrections - revised and improved. Photogrammetric Engineering and Remote Sensing, 62 (9), pp. 1025-1036.

Crane, R.B., 1971, Preprocessing techniques to reduce atmospheric and sensor variability in multispectral scanner data. Proceedings of the 7th International Symposium on Remote Sensing of Environment. Ann Arbor, Michigan, p. 1345.

Çiner, A., Aydar, E., Dirik, K., Rojay, B., Ersoy, O., Sayın, E., Çubukçu, E., Yıldırım, C., and Kutluay, A., 2011. Vertical Anatolian Movement Project Tübitak Report, p. 228.

Delvaux, D., and Sperner, B., 2003. New aspects of tectonic stress inversion with reference to the TENSOR program. Geological Society, London, Special Publications 212(1): pp. 75–100.

Delvaux, D., Moeys, R., Stapel, G., Petit, C., Levi, K., Miroshnichenko, A., Ruzhich, V. and San'kov, V., 1997. Paleostress reconstructions and geodynamics of the Baikal region, central Asia, part 2, Cenozoic rifting, Tectonophysics, 282, pp. 1–38.

Dönmez, M. ve Akçay, A.E., 2010. 1/1000.000 ölçekli Türkiye Jeoloji Haritaları Serisi Çankırı-H30 Paftası, No: 138. Maden Tetkik ve Arama Genel Müdürlüğü, Ankara.

Dönmez, M., Akçay, A.E., Kara, H., Yergök, A.F. ve Esentürk, K., 2008. 1:1000.000 ölçekli Türkiye Jeoloji Haritaları Serisi Kırşehir-İ30 Paftası, No: 90. Maden Tetkik ve Arama Genel Müdürlüğü, Ankara.

Dönmez, M., Bilgin, Z.R., Akçay, A.E., Kara, H., Yergök, A.F. ve Esentürk, K., 2005. 1:1000.000 ölçekli Türkiye Jeoloji Haritaları Serisi Kırşehir-İ31 Paftası, No: 46. Maden Tetkik ve Arama Genel Müdürlüğü, Ankara.

Emre, Ö., Duman, T.Y., Özalp, S., Elmacı, H., Olgun, Ş. ve Şaroğlu, F. 2013. 1/1.250.000 Ölçekli Türkiye Diri Fay Haritası, Maden Tetkik ve Arama Genel Müdürlüğü Özel Yayınlar Serisi-, Ankara, Türkiye.

Esat, K., Çıvgın, B., Kaypak, B., Işık, V., Ecevitoğlu, B., Seyitoğlu, G., 2014. The 2005-2007 Bala (Ankara, Central Turkey) earthquakes: a case study for strike-slip fault terminations. Geologica Acta, 12(1), pp. 71-85.

ESRI (Environmental Systems Research Institute), 2006. ArcGIS Desktop Help 9.2 Geostatistical Analyst.

Ghulam, A., 2009. How to calculate reflectance and temperature using ASTER data, Center for Environmental Sciences at Saint Louis University. http://www.pancroma.com/downloads, 9th December 2018, p. 7.

Gurcay, O.B., 2010. Conference: In: Wagner W., Székely, B. (eds.): ISPRS TC VII Symposium – 100 Years ISPRS, Vienna, Austria, July 5–7, 2010, IAPRS, Vol. XXXVIII, Part 7B.

Gürbüz, M., 1981. İnönü (KB Ankara) Orta Miosendeki Hemicyon sansaniensis (Ursidae) türünün tanımlanması ve stratigrafik yayılımı. Türkiye Jeoloji Kurumu Bülteni 24, pp. 85–90.

Harris Geospatial Solutions, 2017. Updated, 12/31/2013, visited on 19th July 2017.

Jackson, B.B., 1983. Multivariate Data Analysis: An Introduction Irwin, Homewood, Illinois, USA, p. 244.

Karaca, A., 2004. Post-Miocene Deformation of the Area Between Alibey (Kızılcahamam) and Karalar (Kazan) Villages, NW Ankara (Turkey). MSc Thesis, Middle East Technical University, Ankara-Turkey.

Kaymakci, N., 2000. Tectono-stratigraphical Evolution of the Çankırı Basin (Central Anatolia, Turkey). PhD Thesis, Universiteit Utrecht, Utrecht.

Kaymakci, N., White, S.H., and Vandijk, P.M., 2003. Kinematic and structural development of the Çankiri Basin (Central Anatolia, Turkey): a paleostress inversion study, Tectonophysics 364 (1), pp. 85-113.

Ketin, İ., 1966. Anadolu'nun Tektonik Birlikleri. MTA Dergisi, 66, pp. 20-34.

Koçyiğit, A., 1991. Changing stress orientation in progressive intracontinental deformation as indicated by the neotectonics of the Ankara region (NW Central Anatolia). Türkiye Petrol Jeologları Derneği Bülteni 3, pp. 43–55.

Koçyiğit, A., 2008. Ankara'nın Depremselliği ve 2005-2007 Afşar (Bala-Ankara) Depremlerinin Kaynağı. MTA Doğal Kaynaklar ve Ekonomi Bülteni, Sayı 6, Maden Tetkik ve Arama Genel Müdürlüğü, sayfa 1-7, Ankara.

Koçyiğit, A., Rojay, B.F., Cihan, M. and Özacar, A., 2001. The June 6, 2000, Orta (Çankırı, Turkey) Earthquake: Sourced from a New Antithetic Sinistral Strike-slip structure of the North Anatolian Fault System, the Dodurga Fault Zone. "Turkish Journal of Earth Sciences", 10, pp. 69-82.

Koçyiğit, A., Türkmenoğlu, A., Beyhan, A., Kaymakçı, N., Akyol, E., 1995. Post-collisional tectonics of Eskisehir-Ankara-Çankiri segment of Izmir-Ankara-Erzincan suture zone (IAESZ): Ankara orogenic phase, TPJD Bülteni, 6 (1), pp. 69-86.

Leica Geosystems Geospatial Imaging, LLC, 2006. Stereoscopic Analyst User's Guide. United States of America, p. 312.

NASA, Jet Propulsion Laboratory, https://asterweb.jpl.nasa.gov/gdem.asp, 9th January, 2019.

O'Leary, D.W., Friedman, J.D., and Phn, H.A., 1976. Lineament, Linear, Lineation: Some proposed new standard for old terms. Geol. Soc. Amer. Bull., 87, pp. 1463-1469.

Okay, A.I. and Tüysüz, O., 1999, Tethyan sutures of northern Turkey. In "The Mediterranean Basins: Tertiary extension within the Alpine orogen" (eds. B. Durand, L. Jolivet, F. Horváth and M. Séranne), Geological Society, London, Special Publication 156, pp. 475-515.

Ozansoy, F., 1961. Ankara bölgesi fauna teakubu etüdünün esaslı sonuçları [Results of the Study on the faunal essamblages of Ankara region]. Maden Tetkik ve Arama Dergisi 56, pp. 86–95.

Öztan, N.S., 2008, Evaporate mapping in Bala Region (Ankara) by remote sensing techniques. MSc thesis, Geological Engineering Department, Middle East Technical University.

Öztan, N.S., Süzen M.L., 2011. Mapping evaporate minerals by ASTER, International Journal of Remote Sensing, 32 (6), pp. 1651-1673.

PCI Geomatics, PCI Geomatica Online Manual, http://www.pcigeomatics.com/geomatica-help/, 3rd April, 2018.

Rojay B., 2013. Tectonic evolution of the Cretaceous Ankara Ophiolitic Mélange during the Late Cretaceous to pre- Miocene interval in Central Anatolia, Turkey. J. Geodynamics 65, pp. 66–81.

Rojay, B., and Karaca, 2008. A., Post-Miocene Deformation in the South of the Galatean Volcanic Province, NW of Central Anatolia (Turkey). "T. Jour. of Earth Sci.", 17, pp. 653-672.

Sabins, F.F., 1997, Remote Sensing: Principles and Interpretation. 3rd ed., W. H. Freeman & Co., New York, Oxford, p. 494.

Sevin, M. ve Uğuz, M.F., 2011. 1:100.000 ölçekli açınsama nitelikli Türkiye jeoloji haritaları serisi, Çankırı-G30 paftası, No:146. Maden Tetkik ve Arama Genel Müdürlüğü Yayını, Ankara.

Sevin, M. ve Uğuz, M.F., 2011. 1:100.000 ölçekli açınsama nitelikli Türkiye jeoloji haritaları serisi, Çankırı-G31 paftası, No:147. Maden Tetkik ve Arama Genel Müdürlüğü Yayını, Ankara.

Sevin, M., Uğuz, M.F. ve Sarıfakıoğlu, E., 2016. 1:100.000 ölçekli açınsama nitelikli Türkiye jeoloji haritaları serisi, Çankırı-H31 paftası, No:224. Maden Tetkik ve Arama Genel Müdürlüğü Yayını, Ankara.

Seyitoğlu, G., Aktuğ, B., Karadenizli, L., Kaypak, B., Şen, Ş., Kazancı, N., Işık, V., Esat, K., Parlak, O., Varol, B., Saraç, G.,and İleri, İ., 2009. A Late Pliocene – Quaternary Pinched Crustal Wedge in NW Central Anatolia, Turkey: A Neotectonic Structure Accommodating the Internal Deformation of the Anatolian Plate, Geol. Bull. Turkey, 52(1), pp. 121–154.

Seyitoğlu, G., Kazancı, N., Karadenizli, L., Şen, Ş., Varol, B., and Saraç, G., 2004. Neogene tectono-sedimentary development of western margin of Çankırı basin, central Turkey: reply to the comment of Kaymakçı 2003. Terra Nova, 16, pp. 163-165.

Seyitoğlu, G., Kazancı, N., Karakuş, K., Fodor, L., Araz, H., and Karadenizli, L., 1997. Does continuous compressive tectonic regime exist during Late Palaeogene to Late Neogene in NW Central Anatolia, Turkey? Preliminary observations. Turkish Journal of Earth Sciences 6, pp. 77– 83.

Seyitoğlu, G., Kazanci, N., Karadenizli, L., Şen, Ş., Varol, B. and Karabiyikoglu, T., 2000. Rockfall avalanche deposits associated with normal faulting in the NW of Cankiri basin: implications for the postcollisional tectonic evolution of the Neo-Tethyan suture zone. Terra Nova, 12, pp. 245-251.

Şen, Ş. and Rage, J.C., 1979. Çalta (Ankara) Pliyosen Omurgalı Faunası [Pliocene vertebrate fauna of Çalta (Ankara)]. Türkiye Jeoloji Kurumu Bülteni 22, pp. 155–160.

Tatlı, S., 1975. Kızılcahamam Doğu Alanının Jeolojisi ve Jeotermal Enerji Olanakları [Geology and Geothermal Energy Potential of East of Kızılcahamam Area]. Maden Tetkik Arama Enstitüsü report no. 5749.

Tekkaya, İ., 1973. Orta Sinaptaki yeni bir Gazella türü [A new Gazella species in Middle Sinap]. Maden Tetkik ve Arama Dergisi 80, pp. 113–136.

Tekkaya, İ., 1974a. The Bovidae fauna of middle Sinap of Turkey. Türkiye Jeoloji Kurumu Bülteni 17, pp. 173–186.

Tekkaya, İ., 1974b. A new species of Tortonian Anthropoid (primate, mammalia) from Anatolia. Maden Tetkik ve Arama Dergisi 83, pp. 148–165.

Turgut, T., 1978. Kızılcahamam (Ankara-Çeltikçi) ve Çamlıdere Neojen Havzalarının Linyit Olanakları [Lignite Potential of Kızılcahamam (Ankara-Çeltikçi) and Çamlıdere Neogene Basins]. Maden Tetkik Arama Enstitüsü report no. 6173.

Türkecan, A., Hepşen, N., Papak, İ., Akbaş, B., Dinçel, A., Karataş, S., Özgür, İ., Akay, E., Bedi, Y., Sevin, M., Mutlu, G., Sevin, D., Ünay, E. ve Saraç, G., 1991. Seben-Gerede (Bolu)-Güdül- Beypazarı (Ankara) ve Çerkeş-Orta-Kurşunlu (Çankırı) Yörelerinin (Köroğlu Dağları) Jeolojisi ve Volkanik Kayaçların Petrolojisi. Maden Tetkik ve Arama Enstitüsü report no. 9193.

Tüysüz, O., 2005. Neotectonics and Seismicity of Turkey. Lecture notes, p. 70.

Uğuz, M.F. ve Sevin, M., 2011. 1:100.000 ölçekli açınsama nitelikli Türkiye jeoloji haritaları serisi, Kastamonu-F31 paftası, No:145. Maden Tetkik ve Arama Genel Müdürlüğü Yayını, Ankara.

USGS, USGS Earth Explorer, https://earthexplorer.usgs.gov/, 18th October 2017.